Composite Structures 266 (2021) 113776

Contents lists available at ScienceDirect

Composite Structures

journal homepage: www.elsevier.com/locate/compstruct

Predicting buckling-driven delamination propagation in composite laminates: An analytical modelling approach

Anton Köllner [a]

[a] Structures Section, Department of Civil and Environmental Engineering, Imperial College London, London SW7 2AZ, United Kingdom

ARTICLE INFO

Keywords:
Composite laminates
Delamination buckling
Energy release rate
Mixed-mode fracture
Damage tolerance
CAI

ABSTRACT

Robust and efficient predictions of buckling-driven delamination propagation, enabled by a novel analytical modelling approach, are presented. The model considers full mechanical coupling (extension-shear, extension-bend, extension-twist/shear-bend and bend-twist), contact and mode-mixity and thus significantly enhances the capabilities of current analytical approaches. A problem description in cylindrical coordinates enables the evaluation of the energy release rate along the delamination boundary. The model uses an energy formalism to determine the post-buckling deformation and a crack-tip element analysis employing force and moment resultants acting on the delamination boundary to determine the energy release rate. Composite panels with circular thin-film delaminations and various multi-directional stacking sequences are investigated for in-plane compressive loading. Predictions of applied strains causing delamination growth, *i.e.* threshold strain, show good agreement with published experimental data and 3D finite element analysis. A parametric study varying the ratio of delamination size to depth is performed. Based on the findings obtained, governing deformation characteristics of buckling-driven delamination growth are identified and insight into damage tolerant design of composite laminates is obtained, which is of particular interest for compression after impact (CAI) strength of composite structures.

1. Introduction

In modern aircraft, structural composite components are designed against tolerating what is commonly referred to as barely visible impact damage (BVID) [2,34]. Such minor impact scenarios generally cause, besides intra-ply cracks, delaminations in the interfaces of outer plies and thus severely reduce the compressive strength of such components due to buckling-driven delamination propagation [26]. This also applies to compression after impact (CAI) strength, when impact energy is limited to thresholds causing BVID, where delamination buckling and thus buckle-driven delamination growth is the initial and dominant failure mechanism [3]. As a consequence, reliable predictions of the laminate strength associated with buckling-driven delamination propagation is crucial for exploiting the full potential of composite laminates.

Owing to its complexity, the compressive behaviour of damaged composite panels is predominantly studied within the research community by means of finite element analysis (FEA), where growing computational resources enable detailed simulations of both damage caused by impact [24,25,33,34] as well as CAI tests [1,35,36,39]. Another approach is to incorporate experimentally quantified damage parameters within FE simulations [3]. Good agreement with experiments has been documented [25,36], indicating that deformation processes could be adequately modelled. On the other hand, owing to the high computational cost required (*e.g.* see [24,25]), studies focus on certain distinct layups, loading scenarios or damage measures; although practically useful, this can impede some of the fundamental insight into the relation of delamination buckling and buckling-driven delamination growth, as well as exploring optimal stacking sequences that comply with design guidelines.

Owing to their efficiency, such insight can normally be obtained by (semi-)analytical modelling approaches enabling, for instance, parametric studies on the effect of delamination size and depth [19]. While this may prove to be correct for simplified structures, such as delaminated struts, progressing insight from the early works of Kachanov [16] and Chai et al. [7] to recent efforts in [9,19,21,44], significant challenges are present when studying embedded delaminations (2D problems). Typical shortcomings are:

- modelling delamination growth in a globalized manner, *i.e.* increase of length or width of a delamination, instead of locally along the delamination boundary,

E-mail address: a.koellner@imperial.ac.uk

https://doi.org/10.1016/j.compstruct.2021.113776
Received 10 December 2020; Revised 15 January 2021; Accepted 22 February 2021
Available online 3 March 2021
0263-8223/© 2021 The Author(s). Published by Elsevier Ltd.
This is an open access article under the CC BY-NC-ND license (http://creativecommons.org/licenses/by-nc-nd/4.0/).

- neglecting mode-mixity, and
- omitting to model actual delamination growth.

Recently, several works have attempted to resolve aforementioned issues. In study [41], delamination growth in a somewhat semi-localized manner has been considered in the form of discrete extensions of strips approximating the delamination area for a delamination close to the midplane of the laminate. Actual delamination growth in the form of an increase in major or minor axes of elliptical delaminations has been studied in [22,40] for shallow and deep delaminations respectively, where the former outlines that such growth predictions may only be applicable for certain geometries of delaminations. The aforementioned studies either assume that delamination growth is governed by mode I [22,41] or employ simplification by relating mode shapes [22] or geometry [40] to assumed mode II dominated scenarios. It should also be noted regarding embedded delaminations that analytical models have not been used in comprehensive parametric studies analysing different layups, damage size and locations as well as loading scenarios, which highlights the increased complexity of the given problem in comparison with strut (1D) models (*e.g.* [19]).

Thus, the drawback of incorporating mode-mixity into a (semi-) analytical approach appears to be hitherto not resolved. This shortcoming is associated with the requirement of a localized evaluation of the energy release rate (ERR) along the delamination front that, besides some early work in [15] for two points along the boundary, appears to be missing. A first approach by the author towards implementing localized delamination growth and mode-mixity is documented in [18], without providing the generally applicable description as presented herein. The requirement to consider localized delamination growth is highlighted by experimentally observed growth patterns in tests using artificial delaminations [5,20,28] and CAI tests [35,36]. Based on experimental observations made in [29], local buckling of one dominant delamination and thus buckling driven delamination growth is the dominant failure mechanism when composite panels with BVID are loaded under in-plane compression. Moreover, delaminations caused by impact often resemble an elliptical or circular shape [3,8,29].

In the current work, the initiation of buckling-driven delamination growth is investigated for local buckling responses, thus delaminations commonly referred to as thin-film (thickness being $\leqslant$10% of the parent laminate) are considered. Given the aforementioned drawbacks of current analytical models, it is deemed essential to first attempt to fully understand the thin-film problem before extensions to consider global buckling contributions will be pursued. Circular delaminations are studied. Localized delamination growth is considered by employing a problem description in cylindrical coordinates. This enables the evaluation of the energy release rate along the delamination boundary by means of force and moment resultants, alongside an accurate description of buckling mode shapes for arbitrary layups. Following works by Davidson and Schapery [10–12,32], with the aid of an analytical crack-tip element analysis, transformed to the current problem description in cylindrical coordinates, mode-mixity is incorporated within the modelling approach. In-plane uniaxial compression for various stacking sequences and changing depths is studied. Besides the novel modelling approach, the outcome of the work is comprehensive quantitative and qualitative information on the compressive strength of delaminated panels, providing in-depth understanding of buckling-driven delamination growth in composite laminates.

The present article is set out as follows, the novel modelling approach comprising the energy formalism and the crack-tip element analysis is presented in Section 2. A three dimensional (3D) FE model used to verify the modelling approach is presented in Section 3. In Section 4, the model is validated against findings from experiments and a parametric study of several stacking sequences and delamination characteristics is performed. Detailed information on compressive strains causing delamination growth alongside distributions of energy release rates along the delamination boundary are provided, where comparisons with 3D FEA results are made. The results, their applicability and possible design guidelines are discussed in Section 5 and conclusions are drawn in Section 6.

2. Model description

2.1. Geometric model

The geometric model of a composite panel with an embedded delamination (grey shaded area) is shown in Fig. 1. The radius of the circular delamination is denoted by R. Local buckling responses of the sublaminate (*cf.* part ① in Fig. 1) are considered, thus delaminations are deemed to be within the range associated with thin-film delaminations, *i.e.* $a \leqslant 0.1$ with a being the ratio of the thickness of the delaminated region to the overall thickness (t). Moreover, the panel illustrated in Fig. 1 may be regarded as a semi-infinite plate, where loading is applied in the form of far-field compressive in-plane strain ($\varepsilon_0^x, \varepsilon_0^y$), which is directed along respective Cartesian coordinate axes (x, y) implying axial loading to a rectangular parent laminate (*cf.* part ③ in Fig. 1). Even though the model is developed to account for biaxial loading ($\varepsilon_0^x, \varepsilon_0^y$), during the course of the current paper, uniaxial loading will be investigated, with compressive strains being applied in the x-direction only. As specified in Section 2.2, the

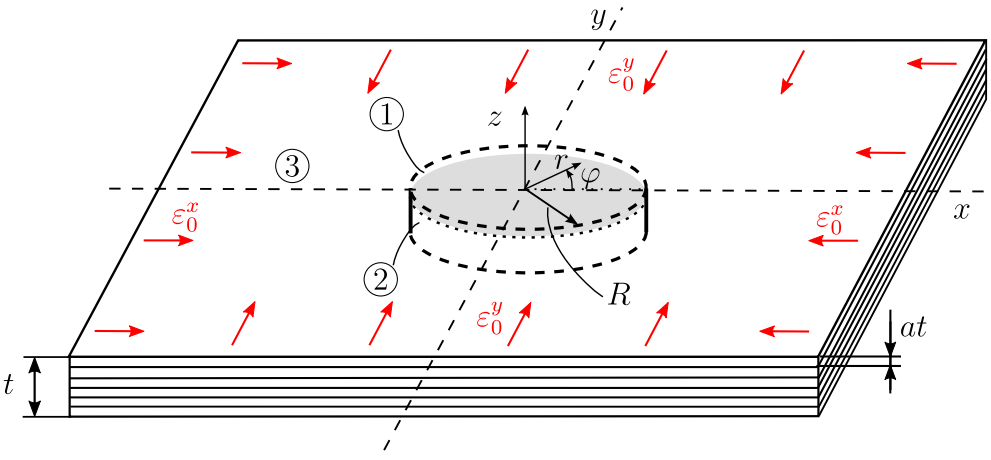


Fig. 1. Geometric model of the delaminated plate.

model description for biaxial loading is used to model the transverse deformation of the parent laminate (part ③) due to the applied compressive loading.

The geometric representation of the sublaminate using cylindrical coordinates (r,φ,z) is beneficial with regards to the adequate modelling of the displacement field as well as the analysis of the energy release rate along the boundary. It should be noted that, owing to the description using cylindrical coordinates, the stiffness tensor of the material (macroscopically homogenised unidirectional (UD) layers) is dependent on the angle φ, *i.e.* $\boldsymbol{C}=\boldsymbol{C}(\varphi)$.

2.2. Energy formalism

Post-buckling deformations of the sublaminate are modelled with the aid of an energy approach employing the Rayleigh–Ritz method. Therefore, the displacement field $\boldsymbol{u}=\boldsymbol{u}(r,\varphi)$ is approximated using trigonometric shape functions, in which both radially symmetric and asymmetric functions are employed, thus:

$$\begin{aligned}
u(r,\varphi) &= \left(\varepsilon_0^x r\cos^2(\varphi)+\varepsilon_0^y r\sin^2(\varphi)\right)\\
&\quad+\sum_{m=1}^{M^u}\sum_{n=0}^{N^u}\sin\left(\frac{m\pi r}{R}\right)\left(a_{mn}^u\sin(2n\varphi)+b_{mn}^u\cos(2n\varphi)\right)\\
v(r,\varphi) &= \left(-\varepsilon_0^x r\cos(\varphi)\sin(\varphi)+\varepsilon_0^y r\cos(\varphi)\sin(\varphi)\right)\\
&\quad+\sum_{m=1}^{M^v}\sum_{n=1}^{N^v}\sin\left(\frac{m\pi r}{R}\right)\left(a_{mn}^v\sin(2n\varphi)+b_{mn}^v\cos(2n\varphi)\right)\\
w(r,\varphi) &= \sum_{m=1}^{M_1^w}\sum_{n=1}^{N_1^w}c_{mn}^w\cos\left(\frac{(2m-1)\pi r}{2R}\right)\cos\left(\frac{(2n-1)\pi r}{2R}\right)\\
&\quad+\sum_{m=1}^{M_2^w}\sum_{n=1}^{N_2^w}\sum_{o=1}^{O^w}\sin\left(\frac{m\pi r}{R}\right)\sin\left(\frac{n\pi r}{R}\right)\left(a_{mno}^w\sin(2o\varphi)+b_{mno}^w\cos(2o\varphi)\right)
\end{aligned}\tag{1}$$

where u, v and w describe the radial, circumferential and out-of-plane displacements respectively, while $a_{mn}^u, b_{mn}^u, a_{mn}^v, b_{mn}^v, c_{mn}^w, a_{mno}^w$ and b_{mno}^w are sets of generalized coordinates which are subsequently summarized in the set q_i. The first terms in the expressions for the radial and circumferential displacement in Eq. (1) refer to the displacements associated with the applied far-field strain. Under uniaxial loading conditions (applied far-field strain ε_0^x only), the transverse extension of the parent laminate is considered, *i.e.* $\varepsilon_0^y=-\nu_{12}^{\text{par}}\varepsilon_0^x$ with ν_{12}^{par} being the major Poisson's ratio of the parent laminate. It should be noted that the far-field strain $(\varepsilon_0^x,\varepsilon_0^y)$ transforms into cylindrical coordinates $(\varepsilon_I^{\text{ff}})$ as follows

$$\{\varepsilon^{\text{ff}}\}=\begin{pmatrix}\varepsilon_{rr}^0\\ \varepsilon_{\varphi\varphi}^0\\ 2\varepsilon_{r\varphi}^0\end{pmatrix}=\begin{pmatrix}c^2 & s^2 & cs\\ s^2 & c^2 & -cs\\ -2cs & 2cs & (c^2-s^2)\end{pmatrix}\begin{pmatrix}\varepsilon_0^x\\ \varepsilon_0^y\\ 0\end{pmatrix}=\begin{pmatrix}c^2\varepsilon_0^x+s^2\varepsilon_0^y\\ s^2\varepsilon_0^x+c^2\varepsilon_0^y\\ -2cs\varepsilon_0^x+2cs\varepsilon_0^y\end{pmatrix},\tag{2}$$

with $c=\cos(\varphi)$ and $s=\sin(\varphi)$. Thus, Eq. (1) fulfils the geometric boundary conditions:

$$\begin{aligned}
u(r=R,\varphi) &= R\left(c^2\varepsilon_0^x+s^2\varepsilon_0^y\right),\\
v(r=R,\varphi) &= R\left(s^2\varepsilon_0^x+c^2\varepsilon_0^y\right),\\
w(r=R,\varphi) &= 0,\\
\nabla_j w(r=R,\varphi) &= 0,
\end{aligned}\tag{3}$$

with $\nabla_j=\left\{\frac{\partial}{\partial r},\frac{1}{r}\frac{\partial}{\partial\varphi}\right\}$.

With the aid of the displacement field defined in Eq. (1), the in-plane strains can be derived in cylindrical coordinates:

$$\begin{pmatrix}\varepsilon_{rr}\\ \varepsilon_{\varphi\varphi}\\ 2\varepsilon_{r\varphi}\end{pmatrix}=\begin{pmatrix}\varepsilon_1\\ \varepsilon_2\\ \varepsilon_6\end{pmatrix}=\{\varepsilon^0\}+z\{\kappa\}=\begin{pmatrix}\frac{\partial u}{\partial r}+\frac{1}{2}\left(\frac{\partial w}{\partial r}\right)^2\\ \frac{1}{r}\frac{\partial v}{\partial\varphi}+\frac{u}{r}+\frac{1}{2}\left(\frac{1}{r}\frac{\partial w}{\partial\varphi}\right)^2\\ \frac{1}{r}\frac{\partial u}{\partial\varphi}+\frac{\partial v}{\partial r}-\frac{v}{r}+\frac{1}{r}\frac{\partial w}{\partial\varphi}\frac{\partial w}{\partial r}\end{pmatrix}+z\begin{pmatrix}-\frac{\partial^2 w}{\partial r^2}\\ -\frac{1}{r^2}\frac{\partial^2 w}{\partial\varphi^2}-\frac{1}{r}\frac{\partial w}{\partial r}\\ -\frac{2}{r}\frac{\partial^2 w}{\partial r\partial\varphi}+\frac{2}{r^2}\frac{\partial w}{\partial\varphi}\end{pmatrix},\tag{4}$$

where $\{\varepsilon^0\}$ and $\{\kappa\}$ are the membrane strains and the curvatures respectively. In Eq. (4), nonlinear von Kármán strains are considered, so that post-buckling paths can be determined.

As aforementioned, the description of the given problem in cylindrical coordinates introduces a dependence of the stiffness tensor on the angle φ, *i.e.* $\boldsymbol{C}=\boldsymbol{C}(\varphi)$. As a consequence, the well-known in-plane (A_{IJ}), coupling (B_{IJ}) and bending (D_{IJ}) stiffness matrices comprised within the Classical Laminate Theory ($\{I,J\}=\{1,2,6\}$) are rewritten employing the coordinate transformation illustrated in Fig. 2a (from the local fibre coordinate system $(\boldsymbol{e}_1,\boldsymbol{e}_2,\boldsymbol{e}_3)$ to the cylindrical coordinate system $(\boldsymbol{e}_r,\boldsymbol{e}_\varphi,\boldsymbol{e}_z)$).

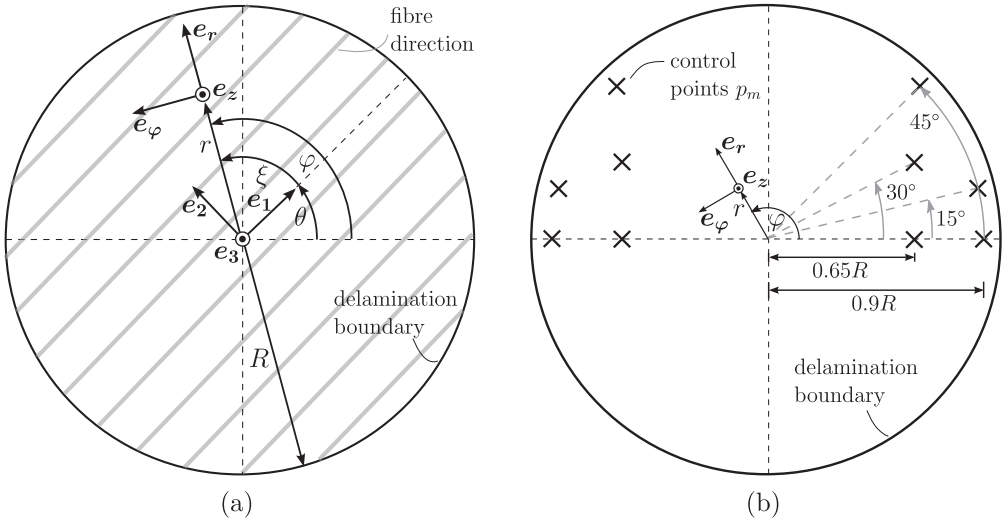


Fig. 2. Model characteristics (top view of delaminated area shown); **(a)** Coordinate transformation from the local fibre coordinate system $(\boldsymbol{e}_1,\boldsymbol{e}_2,\boldsymbol{e}_3)$ to the cylindrical coordinate system $(\boldsymbol{e}_r,\boldsymbol{e}_\varphi,\boldsymbol{e}_z)$; **(b)** configuration of control points p_m enforcing constraint condition $w(r,\varphi)\geqslant 0$.

Throughout the current work, the assumption of plane stress is employed, thus the reduced transformed stiffness matrix $[\bar{Q}](\varphi)$ of each layer of the laminate can be expressed in terms of the reduced stiffness matrix $[Q]$ of the respective unidirectional (UD) layers (assumed to be transversally isotropic) of the laminate, the fibre orientation angle (θ) of the UD ply and the angle φ, using the transformation angle $\xi = \varphi - \theta$, thus:

$$[\bar{Q}](\varphi) = [T][Q][T]^{-\mathrm{T}}, \quad \text{with} \tag{5}$$

$$[T] = \begin{pmatrix} \cos^2\xi & \sin^2\xi & 2\sin\xi\cos\xi \\ \sin^2\xi & \cos^2\xi & -2\sin\xi\cos\xi \\ -\sin\xi\cos\xi & \sin\xi\cos\xi & \cos^2\xi - \sin^2\xi \end{pmatrix}, \text{ and} \tag{6}$$

$$[Q] = \begin{pmatrix} Q_{11} & Q_{12} & 0 \\ Q_{12} & Q_{22} & 0 \\ 0 & 0 & Q_{66} \end{pmatrix}. \tag{7}$$

With the reduced transformed stiffness matrix $\overline{Q}_{IJ}(\varphi)$ provided in Eq. (5), the calculation of the in-plane (A_{IJ}), coupling (B_{IJ}) and bending (D_{IJ}) stiffness matrices follows the well-known formulae from standard textbooks (*e.g.* [31]), *i.e.*

$$\begin{aligned} A_{IJ} &= \sum_{n=1}^{N} \int_{Z^{(n)}} \bar{Q}_{IJ}^{(n)} \mathrm{d}z, \\ B_{IJ} &= \sum_{n=1}^{N} \int_{Z^{(n)}} \bar{Q}_{IJ}^{(n)} z \mathrm{d}z, \quad \text{and} \\ D_{IJ} &= \sum_{n=1}^{N} \int_{Z^{(n)}} \bar{Q}_{IJ}^{(n)} z^2 \mathrm{d}z, \end{aligned} \tag{8}$$

with n referring to the nth layer of the respective part of the panel and $Z^{(n)}$ describing the integration range from the lower to the upper interface of the nth layer.

Since the current work considers local buckling responses, determining the strain energy of the delaminated sublaminate is sufficient for modelling the post-buckling deformations under far field strains ε_0^x and ε_0^y. The strain energy can be calculated by integrating the strain energy density,

$$w_\mathrm{s} = \frac{1}{2}\overline{Q}_{IJ}\varepsilon_I\varepsilon_J, \tag{9}$$

over the volume, yielding

$$W_\mathrm{s} = \frac{1}{2}\int_\varphi \int_r \left(\varepsilon_I^0 A_{IJ}\varepsilon_J^0 + 2\varepsilon_I^0 B_{IJ}\kappa_J + \kappa_I D_{IJ}\kappa_J\right) r \,\mathrm{d}r \,\mathrm{d}\varphi, \tag{10}$$

with the stiffness matrices provided in Eqs. (5) and (8) and the strains given in Eq. (4). Note that in Eq. (10), the in-plane (A_{IJ}), coupling (B_{IJ}) and bending stiffness (D_{IJ}) matrices depend on the angle φ. With the aid of algebraic manipulation performed within the software package Mathematica [42], the strain energy W_s could be determined analytically, thus

$$W_\mathrm{s} = W_\mathrm{s}\left(q_i, \varepsilon_0^x, \varepsilon_0^y, E_{11}, E_{22}, G_{12}, \nu_{12}, t_\mathrm{ply}, R, \theta_n\right), \tag{11}$$

where $E_{11}, E_{22}, G_{12}, \nu_{12}$ are the material parameters of the UD layer (transversally isotropic), t_ply is the thickness of a UD layer, R is the radius of the delamination and $\theta_n = \{\theta_1, \theta_2, \ldots, \theta_N\}$ describes the fibre orientations of the N layers of the sublaminate.

Contact between sublaminate and base laminate (parts ① and ②, *cf.* Fig. 1) is considered by defining control points ($p_m = \{r_m^\mathrm{p}, \varphi_m^\mathrm{p}\}$, with $m = \{1, 2, \ldots, 10\}$) inside the delamination area as visualized in Fig. 2 (b), where the unilateral constraint conditions $w(p_m) \geqslant 0$ are employed by augmenting the strain energy by terms $q_m^\mathrm{p}\left(w(p_m) - c_m^\mathrm{p}\right)$, where q_m^p are Lagrange multipliers representing contact forces and c_m^p are offset parameters describing the out-plane distance between the sublaminate and the base laminate (strictly positive). This represents frictionless hard contact conditions. The energy associated with the constraint condition is denoted by W_p.

Owing to the displacement controlled problem description, the strain energy is the governing functional and the post-buckling response can be determined by the well-known variational principle (*e.g.* [38])

$$\delta W(q_i) = \frac{\partial W}{\partial q_i}\delta q_i = 0 \quad \text{yielding} \quad \frac{\partial W}{\partial q_i} = 0, \tag{12}$$

where the set of nonlinear algebraic equations is solved using the Newton–Raphson method. In Eq. (12), $W = W_\mathrm{s} + W_\mathrm{p}$ and q_i comprises the generalized coordinates employed to describe the displacement field, M Lagrange multipliers and offset parameters, *i.e.*: $q_i = \{a_{mn}^u, b_{mn}^u, a_{mn}^v, b_{mn}^v, c_{mn}^w, a_{mno}^w, b_{mno}^w, q_m^\mathrm{p}, c_m^\mathrm{p}\}$, *cf.* Eq. (1) and Fig. 2b. An initial imperfection in the form of a small out-of-plane displacement of the sublaminate (amplitude of $t_\mathrm{ply}/10$) is considered, which is assumed to be caused by the delamination. The energy contributions associated with the imperfection are deducted from Eq. (10) (*cf.* [17]). As with the strain energy (Eq. (10)), the equilibrium equations (Eq. (12)) are also determined analytically.

With the post-buckling deformation obtained in the form $q_i\left(\varepsilon_0^x, \varepsilon_0^y\right)$ from Eq. (12), the in-plane force and moment resultants can also be determined, which are used to derive the energy release rate along the delamination boundary, which is described next.

2.3. Energy release rate

The description in cylindrical coordinates enables the straightforward determination of force and moment resultants acting on the delamination boundary, which are subsequently employed to determine the energy release rate. Therefore, the crack-tip element analysis following work by Davidson et al. [10,12,32] is adapted herein. Other mixed-mode fracture methods such as proposed in [13,43] may also be employed in the analytical model; however, Davidson et al. [10,12] explicitly account for out-of-plane shear contributions at the delamination front which appears beneficial regarding the intended analysis of arbitrary stacking sequences. A crack-tip element in the context of the current problem description is shown in Fig. 3 highlighting a region of the plate in the vicinity of the delamination front (*cf.* Fig. 1), where Δr_1 and Δr_2 are sufficiently small to neglect nonlinearity but not infinitesimal [12]. Force and moment resultants ($n_{rr}, n_{r\varphi}, m_{rr}$) associated with the sublaminate and the base laminate are indicated by ① and ② respectively.

Fig. 3b shows the free-body diagram of the upper and lower part, exhibiting the crack-tip forces n_ct^r and n_ct^φ as well as the crack-tip moment m_ct. Quantities associated with parts ① and ② but acting in the intact region are indicated by a tilde. With the aid of the free body diagrams in Fig. 3b, the crack-tip forces ($n_\mathrm{ct}^r, n_\mathrm{ct}^\varphi$) and moments ($m_\mathrm{ct}$) can be determined, *i.e.*

$$\begin{aligned} n_\mathrm{ct}^r &= -n_{rr}^{①} + \tilde{n}_{rr}^{①}, \\ n_\mathrm{ct}^\varphi &= -n_{r\varphi}^{①} + \tilde{n}_{r\varphi}^{①}, \\ m_\mathrm{ct} &= -m_{rr}^{①} + \tilde{m}_{rr}^{①} + n_\mathrm{ct}\frac{at}{2}. \end{aligned} \tag{13}$$

It should be noted that crack-tip displacement continuity is enabled by setting $\varepsilon_{\varphi\varphi} = \kappa_{\varphi\varphi} = \kappa_{r\varphi} = 0$ [12], yielding the reduced constitutive behaviour of the crack-tip element:

$$\begin{pmatrix} n_{rr} \\ n_{r\varphi} \\ m_{rr} \end{pmatrix} = \underbrace{\begin{pmatrix} A_{11} & A_{16} & B_{11} \\ & A_{66} & B_{16} \\ \text{sym.} & & D_{11} \end{pmatrix}}_{\boldsymbol{R}} \begin{pmatrix} \varepsilon_{rr} \\ 2\varepsilon_{r\varphi} \\ \kappa_{rr} \end{pmatrix}, \tag{14}$$

with $\boldsymbol{R}$ being the reduced stiffness matrix. The strains ($\varepsilon_{rr}, 2\varepsilon_{r\varphi}$) and curvature ($\kappa_{rr}$) in the intact region (part ③ in Fig. 3a) are obtained by

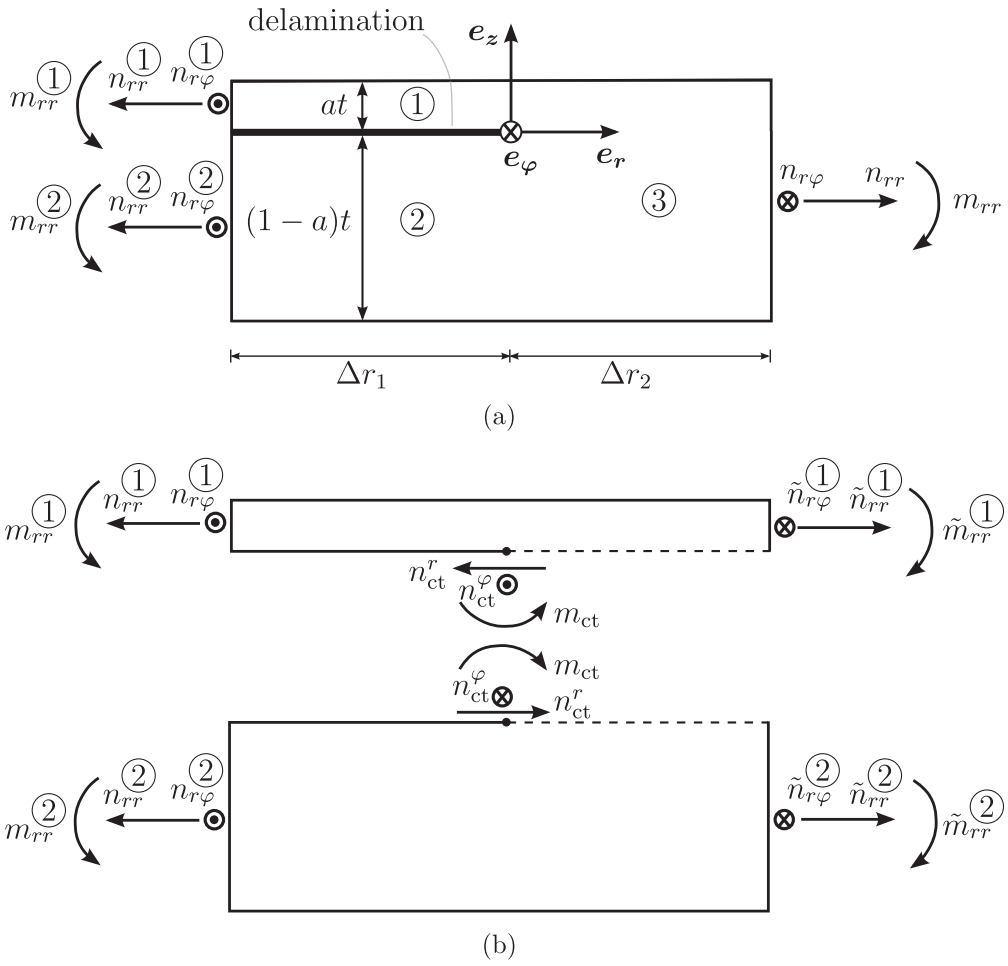


Fig. 3. Crack-tip element; (a) free-body diagram of the crack-tip element; (b) free-body diagrams of the upper and lower part of the crack-tip element using crack-tip forces and moments.

determining the force ($n_{rr}, n_{r\varphi}$) and moment (m_{rr}) resultants from global equilibrium in Fig. 3a, yielding

$$\begin{pmatrix} \varepsilon_{rr} \\ 2\varepsilon_{r\varphi} \\ \kappa_{rr} \end{pmatrix} = \underbrace{\begin{pmatrix} a_{11} & a_{16} & b_{11} \\ & a_{66} & b_{16} \\ \text{sym.} & & d_{11} \end{pmatrix}^{③}}_{\boldsymbol{r}} \begin{pmatrix} n_{rr}^{①} + n_{rr}^{②} \\ n_{r\varphi}^{①} + n_{r\varphi}^{②} \\ m_{rr}^{①} + m_{rr}^{②} + \dfrac{(1-a)t}{2} n_{rr}^{①} - \dfrac{at}{2} n_{rr}^{②} \end{pmatrix}, \tag{15}$$

with $\boldsymbol{r}$ being the reduced compliance matrix obtained by inverting $\boldsymbol{R}$ of part ③. In Eq. (13), the force and moment resultants $\tilde{n}_{rr}^{①}$, $\tilde{n}_{r\varphi}^{①}$ and $\tilde{m}_{rr}^{①}$ are determined by employing the strains in the intact region (*cf.* Eq.(15)) considering the offset of the neutral axes of parts ③ and ①, *i.e.*: $(1-a)t/2$, with the reduced stiffness matrix of part ① (sublaminate), thus

$$\begin{pmatrix} \tilde{n}_{rr} \\ \tilde{n}_{r\varphi} \\ \tilde{m}_{rr} \end{pmatrix}^{①} = \begin{pmatrix} A_{11} & A_{16} & B_{11} \\ & A_{66} & B_{16} \\ \text{sym.} & & D_{11} \end{pmatrix}^{①} \begin{pmatrix} \varepsilon_{rr} + \dfrac{(1-a)t}{2}\kappa_{rr} \\ 2\varepsilon_{r\varphi} \\ \kappa_{rr} \end{pmatrix}. \tag{16}$$

The force and moment resultants of parts ① and ② (*cf.* Eq. (13)) are obtained using the respective in-plane, coupling and bending stiffness matrices and employing strains and curvatures at the delamination boundary determined with the aid of the equilibrium path $q_i(\varepsilon_0^x, \varepsilon_0^y)$, where part ② is under far-field strain only (thin-film assumption).

The crack-tip forces and moment (*cf.* Eq. (13)) act to close a virtually extended delamination front, similar to the virtual crack closure technique (VCCT) employed in FEA [23]. Thus, the total energy release rate can be obtained by

$$G = \frac{1}{2\Delta r_2}\left(n_{\text{ct}}^{r}\Delta u + n_{\text{ct}}^{\varphi}\Delta v + m_{\text{ct}}\Delta\beta\right), \tag{17}$$

where Δr_2 is the length of the newly generated delamination (crack) while $\Delta u, \Delta v$ and $\Delta\beta$ are the relative displacements (normal and shear) and angle to (virtually) close the crack.

The displacements Δu and Δv as well as the angle $\Delta\beta$ can be obtained by considering a statically equivalent loading configuration, where crack-tip forces and moments act on the neutral plane of the upper and lower part rather than at the crack-tip (*cf.* [32]). Thus, strains and curvatures required to evaluate the relative displacements and rotations are given by

$$\begin{pmatrix} \varepsilon_{rr} \\ 2\varepsilon_{r\varphi} \\ \kappa_{rr} \end{pmatrix}^{①} = \begin{pmatrix} a_{11} & a_{16} & b_{11} \\ & a_{66} & b_{16} \\ \text{sym.} & & d_{11} \end{pmatrix}^{①} \begin{pmatrix} n_{\text{ct}}^{r} \\ n_{\text{ct}}^{\varphi} \\ m_{\text{ct}} - \frac{at}{2} n_{\text{ct}}^{r} \end{pmatrix} \tag{18}$$

and

$$\begin{pmatrix} \varepsilon_{rr} \\ 2\varepsilon_{r\varphi} \\ \kappa_{rr} \end{pmatrix}^{②} = \begin{pmatrix} a_{11} & a_{16} & b_{11} \\ & a_{66} & b_{16} \\ \text{sym.} & & d_{11} \end{pmatrix}^{②} \begin{pmatrix} -n_{\text{ct}}^{r} \\ -n_{\text{ct}}^{\varphi} \\ -m_{\text{ct}} - \frac{at}{2} n_{\text{ct}}^{r} \end{pmatrix}. \tag{19}$$

With Eqs. (18) and (19), the relative displacements over the extended crack length Δr_2, *i.e.*:

$$\begin{aligned}\frac{\Delta u}{\Delta r_2} &= \varepsilon_{rr}^{①} - \frac{at}{2}\kappa_{rr}^{①} - \varepsilon_{rr}^{②} - \frac{(1-a)t}{2}\kappa_{rr}^{②}\\ \frac{\Delta v}{\Delta r_2} &= 2\varepsilon_{r\varphi}^{①} - 2\varepsilon_{r\varphi}^{②}\\ \frac{\Delta \beta}{\Delta r_2} &= \kappa_{rr}^{①} - \kappa_{rr}^{②},\end{aligned} \tag{20}$$

can be determined and replaced in Eq. (17) yielding

$$G = \frac{1}{2}\left(c_{11}\left(n_{ct}^{r}\right)^2 + c_{22}\left(m_{ct}\right)^2 + c_{33}\left(n_{ct}^{\varphi}\right)^2 + c_{12}n_{ct}^{r}m_{ct} + c_{13}n_{ct}^{r}n_{ct}^{\varphi} + c_{23}m_{ct}n_{ct}^{\varphi}\right), \tag{21}$$

where coefficients c_{ij} contain the compliances of both parts and thickness measures only. The coefficients c_{ij} are provided in Appendix A. Note that these are the same as in [12] with the exception of a sign change in the coupling compliances, which relates to the opposed thickness (z) direction considered herein.

As pointed out in [10], a non-singular field approach regarding mode-mixity provides good agreement with experiments and 3D FEA for carbon/graphite epoxy laminates, where all configurations falling under thin-film considerations ($a \leq 0.1$, *cf.* Fig. 1) are associated with a mode-mix parameter $\Omega = 24^\circ$ [10]. As described in [11,12], mode I and mode II contributions of the energy release rate (ERR) are given by

$$\begin{aligned}G^{\mathrm{I}} &= \tfrac{1}{2}\left(-\sqrt{c_{11}}n_{ct}^{r}\sin(\Omega) + \sqrt{c_{22}}m_{ct}\cos(\Omega+\Gamma)\right)^2\\ G^{\mathrm{II}} &= \tfrac{1}{2}\left(\sqrt{c_{11}}n_{ct}^{r}\cos(\Omega) + \sqrt{c_{22}}m_{ct}\sin(\Omega+\Gamma)\right)^2,\end{aligned} \tag{22}$$

with $\Gamma = \arcsin\left(c_{12}(c_{11}c_{22})^{-1/2}\right)$. Applicability of Eq. (22) to multidirectional laminates is shown in [10]. Mode III ERR is obtained by subtracting Eq. (22) from Eq. (21), *i.e.* $G^{\mathrm{III}} = G - G^{\mathrm{I}} - G^{\mathrm{II}}$. Note that besides the crack-tip forces and moments, the material parameters in c_{ij} depend on the angle φ introduced by the problem description in cylindrical coordinates.

3. Finite element model

A three dimensional geometrically non-linear finite element analysis (3D FEA) is performed within Abaqus [37] to verify the analytical modelling approach. The thin-film problem is simulated by considering delaminations complying with the condition $a \leq 0.1$ (*cf.* Fig. 1) and suppressing any out-of-plane displacements of the bottom face of the plate. The FE model consists of two parts containing the layers above and below the interface exhibiting the delamination, respectively. The lower thicker part is built up with two regions: the lower region, deemed outside the fracture process zone, is modelled using continuous shell elements with one element per thickness. The upper region of the lower part is modelled using solid elements (CD8R) with one element per layer thickness. The part above the delamination is also modelled with solid elements (CD8R), however more elements per layer thickness are required to model the bending deformation precisely during the processes of critical buckling and post-buckling. Three elements per layer thickness were found as being the optimal choice by analysing critical buckling and post-buckling responses in pre-tests. The through-the-thickness composition of the FE model is visualized in Fig. 4 (bottom left) alongside the global (both parts assembled) FE model (left), a top view of the mesh of the upper region (top right) and a magnified view of the delamination front (bottom right).

Mesh refinement to an element size (l_{FE}) of 0.15 mm around the delamination front in both parts is performed, which is in the range of $0.1t_{\mathrm{ply}} < l_{\mathrm{FE}} < t_{\mathrm{ply}}$ providing reliable mode decomposition in the VCCT [23], with t_{ply} being the thickness of a unidirectional (UD) layer. The delaminated region (*cf.* Fig. 1 sublaminate part ①) is modelled with an element size of 0.8 mm (*cf.* right side in Fig. 4). A larger element size (3 mm) is sufficient for the outer region of the plate undergoing far-field in-plane loading only. Bonding of both parts is set up by assigning nodes outside the delaminated region to the VCCT employing a B-K law fracture criterion [4] using respective critical energy release rates for mode I, II and III, which are provided in Table 3 alongside the material parameters used. Frictionless hard contact as considered in the analytical model is configured. Loading in the form of end-shortening is applied to the plate by configuring kinematic coupling between the right edges/surfaces of both parts (*cf.* Fig. 4) and a reference point, where the latter follows a monotonically increasing displacement up to the initiation of delamination growth, *i.e.* $G_{\mathrm{norm}} = 1$. The opposite side of the loading edge/surface is modelled suppressing in-plane displacements in the loading direction (x-direction) but allowing transverse displacements. For all other edges, in-plane displacements are enabled allowing the plate to undergo transverse expansion. Rotations and out-of-plane displacements are

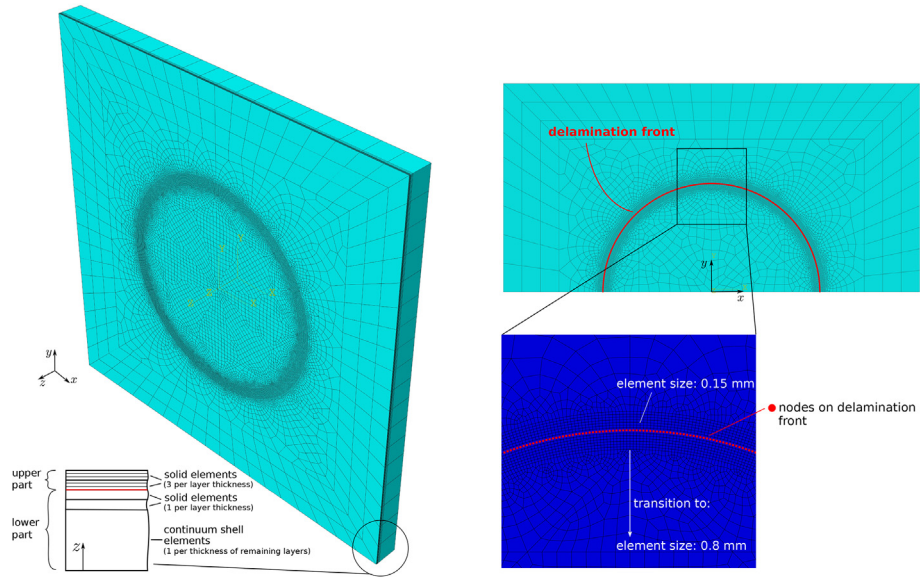


Fig. 4. FE model.

suppressed on all edges modelling clamped boundary conditions. A minor out-of-plane imperfection load is applied to the midpoint of the upper part of the model to enable tracing the post-buckling path; the load is set to zero once buckling occurs.

Depending on the size of the delamination studied (*cf.* Section 4), the FE model consists of approximately 150,000 (smaller delaminations) to 200,000 (larger delaminations) elements requiring 7–14 GB of memory and roughly an 1-h run time on an 8 core Intel(R) i7 processor.

4. Results

First, the model is validated in Section 4.1 by comparing post-buckling deformation and strains causing delamination growth to experimental findings provided in the literature. Subsequently, results of a parametric study focussing on three distinct types of laminates are presented in Section 4.2.

4.1. Validation

Regarding the model description in Section 2.2, based on pre-tests evaluating the post-buckling behaviour and, in particular, the behaviour of the energy release rate against 3D FEA and experiments, a total of 240 generalized coordinates are employed in the analytical model that relate to Eq. (1) as follows: $M^u = M^v = 10,\ N^u = N^v = 5,\ M_1^w = N_1^w = M_2^w = N_2^w = 3,\ O^w = 2$. In addition to the validation provided in this section, the capability of the trigonometric shape functions to adequately approximate the displacement field of the sublaminate is highlighted in Section 4.2.1 in Fig. 7 showing buckling shapes deep in the post-buckling response. The choice of generalized coordinates is discussed in Section 5.1.

In Figs. 5a and 5b, post-buckling deformation in terms of compressive applied load against midpoint deflection of the sublaminate (w_{mid}) is compared to cases studied in Refs. [20,27], where in [20] compressive strain (ε_0) and in [27] compressive force (P) is provided. Deformation paths up to the load causing delamination growth in the respective experiments are shown.

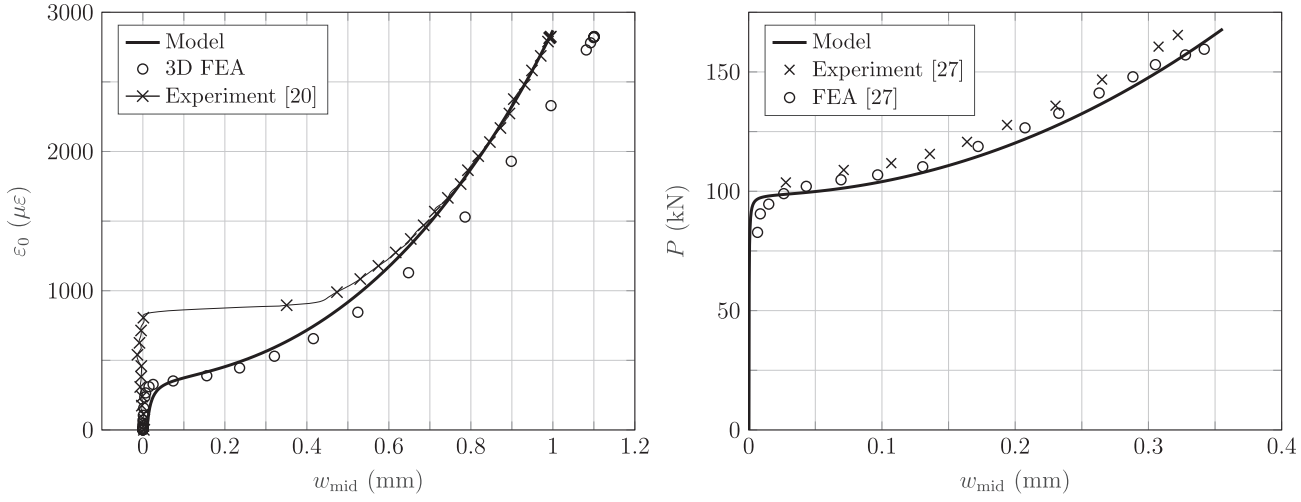
In Fig. 5a, a quasi-isotropic laminate is investigated with the layup of the sublaminate being [0/45], exhibiting full mechanical coupling; Fig. 5b considers a cross-ply laminate with the delaminated region having a symmetric layup ([90/0/90]). In both studies, anti-buckling guides are used to impede global bending contributions. An artificial circular delamination is inserted in the layups at depths $a = 1/12$ [20] and $a = 1/16$ [27]. Both comparisons show that the analytical model presented is capable of tracing the post-buckling path of fully coupled sublaminates ($B_{IJ} \neq 0, A_{I6} \neq 0, D_{I6} \neq 0$, Fig. 5a) and and configurations exhibiting strong contact between sublaminate and base laminate (Fig. 5b). Buckling strains/loads basically coincide for both cases when compared to FEA. The delayed buckling response shown for the experiment in Fig. 5a is discussed in detail in [20], where it is argued that this relates to minor negative out-of-plane displacements and small misalignments of the specimen, causing moments on the delamination boundary acting to close the buckle. Following the delayed buckling, the post-buckling path of the experiment follows precisely the prediction of the analytical model. However, as described in [20] by analysing digital image correlation (DIC) images, due to the test configuration, minor negative out-of-plane displacements of the base laminate are present (≈ -0.05 mm), which upon complete suppression would bring the experimental curve closer to the 3D FEA. Compared to the analytical model, the 3D FEA shows 10% larger midpoint deflection at the initiation of delamination growth. In Fig. 5b, post-buckling paths of the model, FEA and experiment agree well throughout the deformation process.

Next, applied strains causing delamination growth, commonly referred to as *threshold strains* ε^{th}, are compared to results documented in Refs. [20,27]. These comparisons alongside predictions from the 3D FEA described in Section 3 are provided in Table 1.

In Table 1, deviations between the analytical model and experiments are provided in the last column (Δ), where deviations are calculated to the respective lower or upper value, if a range is shown. Predictions of the model show very good agreement for cases

Table 1
Comparison of applied strains causing delamination growth (threshold strains ε^{th}); (*) – result from [27] using shell elements.

Layup	Ref. Expt.	Threshold strain ε^{th} ($\mu\varepsilon$)			Δ (%)
		Model	3D FEA	Expt.	
[45/-45]	[20]	7780	6890	7040–7130	9
[0/90/90]	[20]	3960	3400	3680	7
[0/45]	[20]	3580	2830	2770–3080	16
[90/0/90]	[27]	3510	3200*	3300	6



(a) ε_0 vs. w_{mid}, sublaminate: [0/45] (b) P vs. w_{mid}, sublaminate: [90/0/90]

Fig. 5. Comparisons of post-buckling deformation.

[45/-45], [0/90/90] and [90/0/90] with deviations within 9%. These cases cover configurations which exhibit extension-twist (shear-bend) coupling and require large applied strains ([45/-45]), extension-bend coupling ([0/90/90]) and contact between sublaminate and base laminate (all cases). Case [0/45] exhibits full mechanical coupling (extension-shear, extension-bend, extension-twist and bend-twist) and shows the lowest threshold strain of all cases. A deviation of 16% between the analytical model and experiments is shown for this case in Table 1, which is analysed in detail in Section 4.2. In-depth analysis of the experiments and comparison to the model is provided in the accompanying study presented in [20], where buckle-driven delamination propagation in quasi-isotropic laminates is investigated using DIC images and ultrasonic C-scans, evaluating the deformation of the buckle, threshold strain predictions and the direction of the onset of delamination growth.

4.2. Parametric study

Since quasi-isotropic laminates are most commonly used in applications in the aircraft/aerospace industry (*e.g.* see [20,26,35]), these layups are studied herein considering a laminate with 32 layers. Various stacking sequences are considered which are deemed to be most suitable regarding their compressive strength and most commonly used studying the CAI strength and BVID (*e.g.* see [35]). These layups also exhibit different types of mechanical coupling. Delamiantions between the second and third, as well as the third and fourth layer (from the top surface) are studied, *i.e.* $a = \{1/16, 3/32\}$ (*cf.* Fig. 1). The stacking sequences with their respective layup of the sublaminate (delaminated region) are provided in Table 2.

As shown in Table 2, three types of sublaminates are studied: type A – extension-twist/shear-bend coupling ($B_{I6} \neq 0$) but no extension-shear and bend-twist coupling ($A_{I6} = 0$ and $D_{I6} = 0$); type B – full mechanical coupling ($A_{I6} \neq 0, B_{IJ} \neq 0, D_{I6} \neq 0$); type C – extension-shear and bend-twist coupling ($A_{I6} \neq 0, D_{I6} \neq 0$) but zero coupling stiffness ($B_{IJ} = 0$). The material parameters are taken from [20] and are provided in Table 3 alongside the dimensions investigated. Note that parameters E_{33}, G_{23}, ν_{23} are only used for the 3D FEA. Regarding the delamination radii considered, case 1 refers to $a = 1/16$ and case 2 to $a = 3/32$. Given the range of delamination radii and the ply thickness (t_{ply}), cases investigated are within the range of a diameter-to-thickness ratios (χ) of 41 – 102. In total, 41 configurations are investigated with the analytical model.

Table 2
Laminate and sublaminate stacking sequences.

Laminate	Sublaminate	Type
$[45/-45//0/90/(45/-45/0/90)_3]_s$	$[45/-45]$	Type A
$[45/0//-45/90/(45/0/-45/90)_3]_s$	$[45/0]$	Type B
$[45_2//-45_2/90_2/45_2/-45_2/0_2/90_2]_s$	$[45_2]$	Type C
$[45/0/-45//90/(45/0/-45/90)_3]_s$	$[45/0/-45]$	Type A
$[45/-45/0//90/(45/-45/0/90)_3]_s$	$[45/-45/0]$	Type B

Table 3
Material (AS4/8552 lamina) parameters (taken from [20]) and dimensions.

Material parameters		Dimensions	
E_{11}	128 GPa	t_{ply}	0.196 mm
$E_{22} = E_{33}$	10.3 GPa	a	$\{1/16, 3/32\}$
$G_{12} = G_{13}$	6 GPa	R (case 1)	$\{8, 10, 12, 14, 16, 18, 20\}$ mm
G_{23}	3.43 GPa	R (case 2)	$\{12, 14, 16, 18, 20, 22, 24, 26, 28\}$ mm
ν_{12}	0.3	$\chi = 2R/(at)$	≈41–102
ν_{23}	0.5		
G_c^{I}	0.268 N/mm		
$G_c^{\text{II}} = G_c^{\text{III}}$	0.738 N/mm		

Uniaxial applied compressive strain, *i.e.* $\varepsilon_0^x = \varepsilon_0$, is considered throughout the parametric study, where the parent laminate can undergo transverse deformation. This is enabled by setting $\varepsilon_0^y = -\nu_{12}^{\text{par}}\varepsilon_0$ (*cf.* Fig. 1 and Eq. (1)), with ν_{12}^{par} being the major Poisson's ratio of the intact (parent) laminate ($\nu_{12}^{\text{par}} \approx 0.299$). In the analytical modelling approach and the 3D FEA, the critical energy release rate (ERR) is determined employing the B-K law [4],

$$G_c^{\text{mix}} = G_c^{\text{I}} + \left(G_c^{\text{II}} - G_c^{\text{I}}\right)\left(\frac{G^{\text{II}} + G^{\text{III}}}{G^{\text{I}} + G^{\text{II}} + G^{\text{III}}}\right)^{\eta}$$

with $\eta = 1.75$ and the material parameters ($G_c^{\text{I}}, G_c^{\text{II}}$) provided in Table 3. Despite its empirical nature, the B-K law was chosen in the current study due to its explicit consideration of mode III contributions and its readily implementation. However, other criteria as proposed in [14,28] may also be applied.

Subsequently, findings of the parametric study are presented. Therefore, first characteristic buckling responses are illustrated (Section 4.2.1), which will aid evaluating subsequently results for threshold strains and the behaviour of the ERR shown in Section 4.2.2.

4.2.1. Delamination buckling

Post-buckling deformation of the sublaminates is investigated by analysing applied strain against midpoint deflection as well as buckling shapes at the initiation of delamination growth. To evaluate whether the stacking sequence of the sublaminate affects the predictions of the analytical model, type A and type B layups are considered for configurations of different diameter-to-thickness ratios χ, which will also be analysed in Section 4.2.2. Fig. 6 shows the post-buckling paths in terms of applied strain against midpoint deflection for delaminated regions having the stacking sequence [45/-45] (type A, blue lines and symbols) and [45/-45/0] (type B, red lines and symbols).

The values of χ shown in Fig. 6 correspond to $R = \{12, 20\}$ mm for [45/-45] and $R = \{20, 28\}$ mm for [45/-45/0]. Results of corresponding 3D FEA simulations are provided by symbols "○". Post-buckling paths are shown up to the deformation state predicted to cause delamination growth. Fig. 6 shows good agreement between the analytical model and FEA, where buckling strains almost coincide and post-buckling deformation predicted by the 3D FEA are slightly softer, which is expected given that the analytical model considers 2D deformations without out-of-plane shear. It appears that the post-buckling deformation in terms of midpoint deflection is not affected by the type of stacking sequence underlining that full mechanical coupling is adequately considered in the model.

It should be noted that during post-buckling contact between sublaminate and base laminate occurs for all cases shown, altering the initial buckling shape (even if the initial buckling response does not cause contact) with more pronounced effects at larger χ. This behaviour has

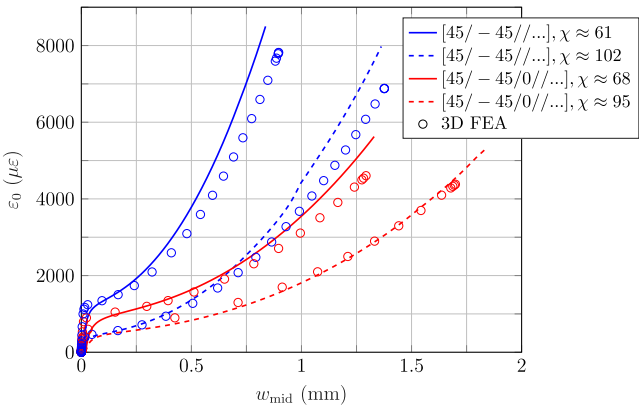


Fig. 6. Comparisons of post-buckling deformation.

also been observed in experiments [20] causing a more localized buckling shape. For instance, the occurrence of contact can be seen by taking a closer look at case [45/-45] with $\chi \approx 102$ at approximately $4500\,\mu\varepsilon$ exhibiting a knee in the post-buckling path with subsequent minor flattening of the curve.

Such localized buckling shapes are visualized in Fig. 7 for sublaminate [45/-45] (Figs. 7a and 7b) comparing out-of-plane displacements of the buckle between the model and FEA at respective applied strains causing delamination growth (ε^{th}). In Figs. 7a and 7b, it is clearly visible that the buckle does not spread over the entire delaminated region but localizes with approximately half the length in longitudinal direction but fully spread in transverse direction. As described in [20] evaluating experimental DIC images, the buckle rotates from an initial off-axis position (regarding the transverse direction) to a more transversely aligned shape as shown in Figs. 7a and 7b, where such rotations are still slightly visible in Fig. 7a.

Smaller diameter-to-thickness ratios (χ), as exemplarily visualized by sublaminate [45/-45/0] with $\chi = 68$, do not exhibit such a pronounced localized buckling deformation. Moreover, delamination growth occurs before the buckle encounters the aforementioned transversely aligned position. The slightly rotated buckling shape with a transverse alignment of the buckle of $< 90^\circ$ is caused by the 0° layer added to the balanced angle ply sublaminate [45/-45]. Note that cross-ply and 0°-unidirectional laminates do not exhibit such behaviour (owing to $A_{I6} = B_{I6} = D_{I6} = 0, I = \{1, 2\}$), where the buckle would move from an initial radially symmetric shape to a more localized transversely aligned shape.

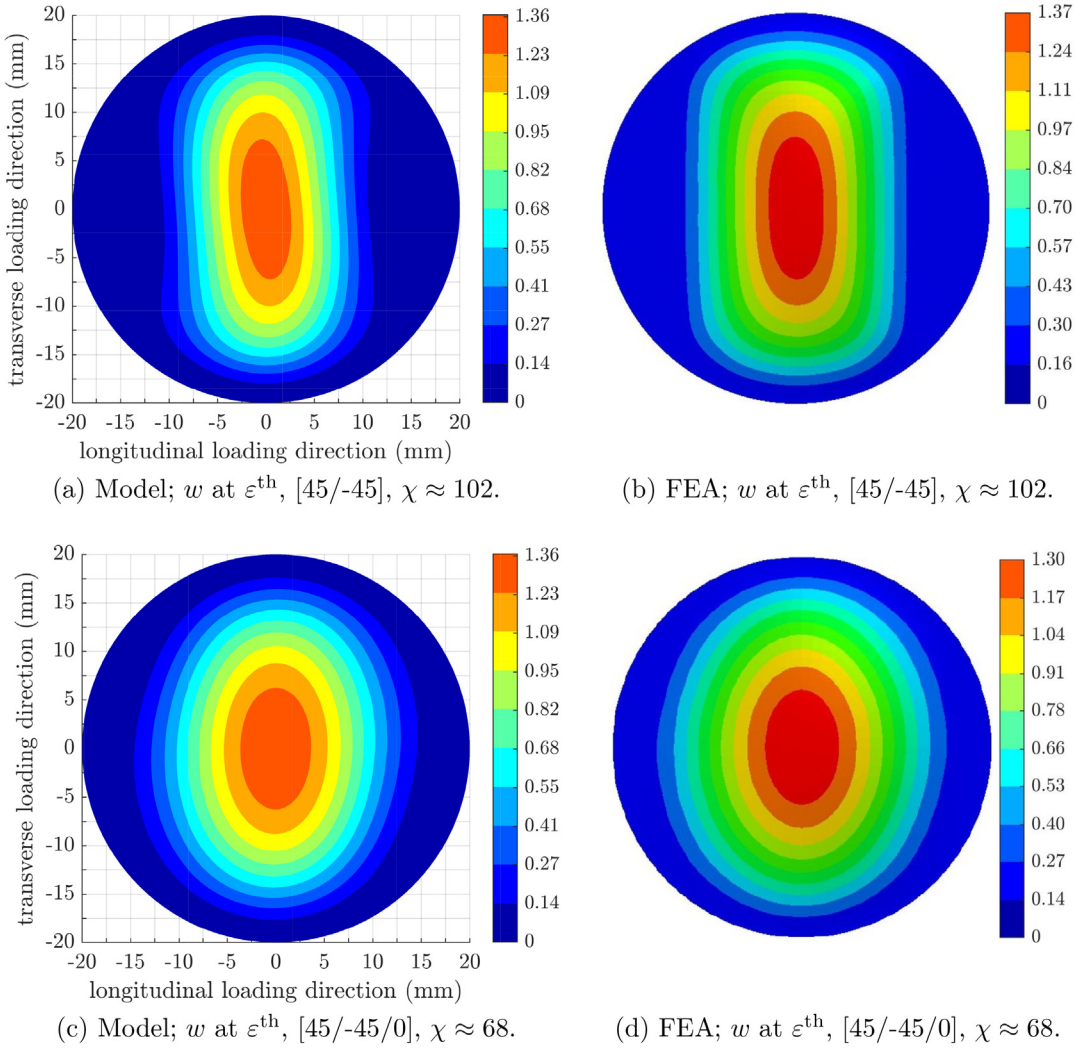
Besides the midpoint deflection and the orientation of the buckle, deformations in the vicinity of the delamination boundary are of importance when analysing the delamination growth behaviour, in particular if a force/stress based approach is employed. Comparing buckling shapes provided in Fig. 7, slightly larger out-of-plane displacements are visualized for the FEA, underlining the aforementioned softer behaviour compared to the analytical model, where larger χ are deemed to increase the discrepancy.

Next, threshold strain predictions and the behaviour of the ERR are described for each type of sublaminate using the configurations considered in this section.

4.2.2. Threshold strain and energy release rate

For each type of sublaminate (type A, type B, type C), threshold strain predictions for the diameter-to-thickness ratios (χ) considered are presented alongside a breakdown of the behaviour of the ERR and its components along the delamination boundary. The results are compared to 3D FEA, where simulations have been performed for $R = \{8, 12, 16, 20\}$ mm for $a = 1/16$ (sublaminates with two layers) and $R = \{12, 16, 20, 24, 28\}$ mm for $a = 3/32$ (sublaminates with three layers).

Fig. 8 summarizes the delamination growth behaviour for type A sublaminates ($A_{I6} = D_{I6} = 0, B_{I6} \neq 0$, with $I = \{1, 2\}$). Threshold strain



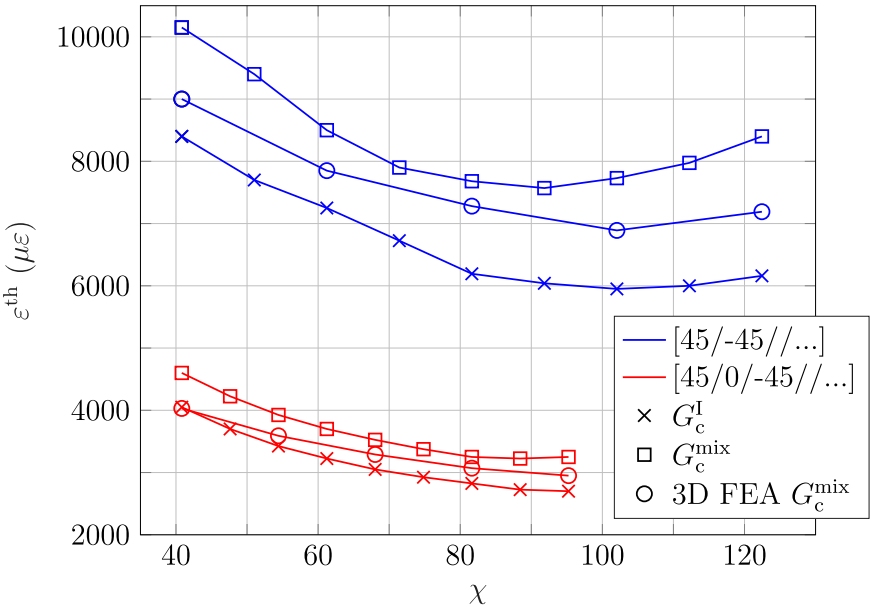
(a) Model; w at ε^{th}, [45/-45], $\chi \approx 102$.

(b) FEA; w at ε^{th}, [45/-45], $\chi \approx 102$.

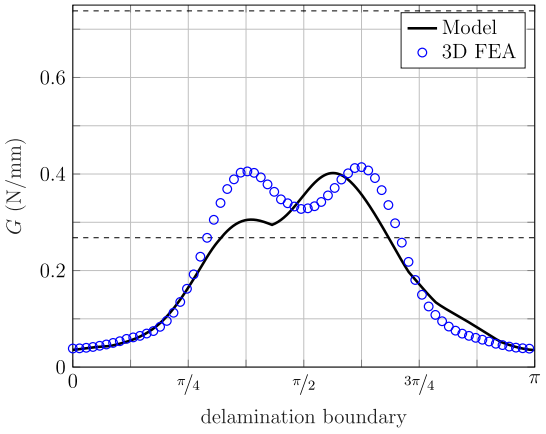
(c) Model; w at ε^{th}, [45/-45/0], $\chi \approx 68$.

(d) FEA; w at ε^{th}, [45/-45/0], $\chi \approx 68$.

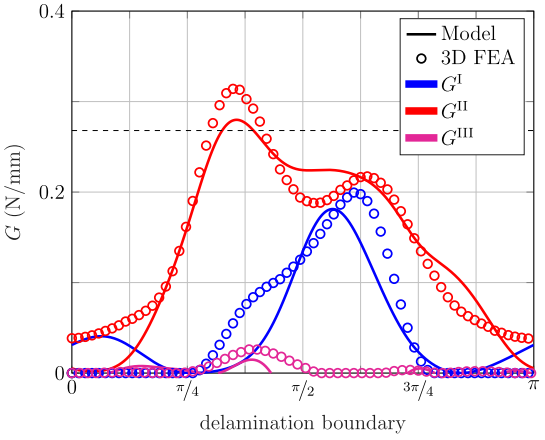
Fig. 7. Buckling shapes (out-of-plane displacement w of the buckle/sublaminate) at initiation of delamination growth ε^{th}.



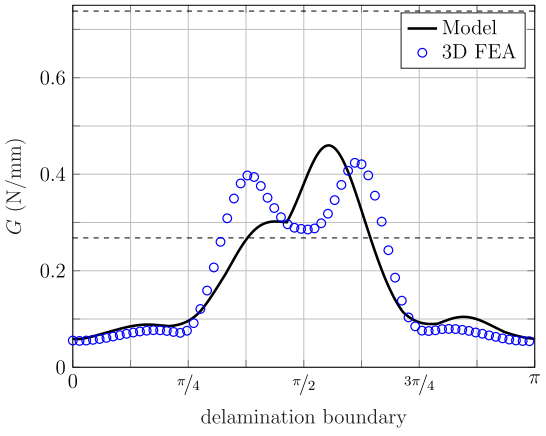
(a) Threshold strain $\varepsilon^{\mathrm{th}}$ predictions against χ for type A.



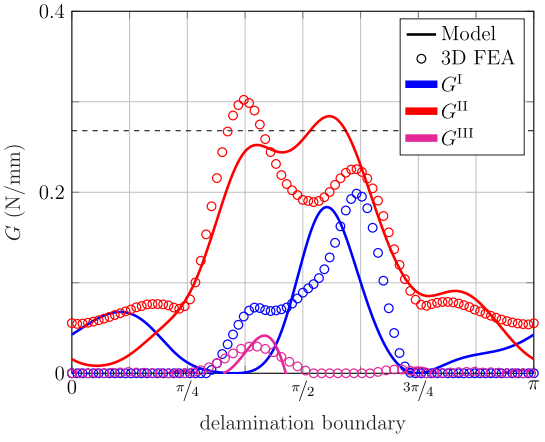
(b) $G(\varphi)$ at $\varepsilon^{\mathrm{th}}$, [45/-45], $\chi \approx 61$.



(c) $G^{\mathrm{I}}, G^{\mathrm{II}}, G^{\mathrm{III}}$ at $\varepsilon^{\mathrm{th}}$, [45/-45], $\chi \approx 61$.



(d) $G(\varphi)$ at $\varepsilon^{\mathrm{th}}$, [45/-45], $\chi \approx 102$.



(e) $G^{\mathrm{I}}, G^{\mathrm{II}}, G^{\mathrm{III}}$ at $\varepsilon^{\mathrm{th}}$, [45/-45], $\chi \approx 102$.

Fig. 8. Delamination growth behaviour of type A sublaminates, $\chi = \frac{2R}{at}$.

(ε^{th}) predictions for the range of χ studied are shown in Fig. 8a. Representative for the capability to describe the behaviour of type A sublaminates, the behaviour of the ERR and its components (mode I, mode II, mode III) at initiation of delamination growth is provided in Figs. 8b–e for the stacking sequence [45/-45] with $\chi \approx \{61, 102\}$.

In Fig. 8a, three lines (linear interpolated) visualize threshold strain predictions for the range of χ for each sublaminate. Symbols □ and ○ represent threshold strain predictions for the analytical model and the 3D FEA respectively, considering mode-mixity employing the B-K law (*cf.* Eq. (23)), thus $G = G_c^{mix}$ at ε^{th}. Furthermore, symbols × indicate when $G = G_c^{I}$ in the analytical model, mimicking a conservative mode I fracture criterion.

Fig. 8a shows good agreement between analytical model and 3D FEA, where threshold strain predictions of FEA lie between G_c^{I} and G_c^{mix} of the analytical model for all configurations, with deviations of 5 % to 12 % for [45/-45] and 6 % to 13 % for [45/0/-45] (considering G_c^{mix}). Moreover, the qualitative behaviour agrees well between the model and FEA. In order to verify the increase in threshold strain predictions seen for [45/-45] at larger χ, the range of configurations studied has been extended for this stacking sequence only ($\chi_{max} = 122$). A detailed overview of threshold strain predictions and respective deviations are provided in Table 4 for all stacking sequences and configurations.

The behaviour of the total ERR along the delamination boundary, *i.e.* $G(\varphi)$ at R (*cf.* Fig. 1), at the respective threshold strain ε^{th} is visualized in Figs. 8b and 8 for smaller ($\chi \approx 61$) and larger ($\chi \approx 102$) diameter-to-thickness ratios, respectively. Very good agreement between the analytical model and 3D FEA is shown, where both exhibit a wide spread distribution of significant magnitudes of ERR from approximately angles $\pi/4$ to $3\pi/4$, with larger χ causing a slight narrowing of this span. The maximum ERR, which is also the critical ERR (G_c^{mix}) for this case, almost coincides with the FEA prediction for $\chi \approx 61$ (model: $G_c^{mix} \approx 0.40$; 3D FEA: $G_c^{mix} \approx 0.41$) and deviate slightly for $\chi \approx 102$ (model: $G_c^{mix} \approx 0.46$; 3D FEA: $G_c^{mix} \approx 0.43$). The double-peak behaviour of the ERR predicted by the 3D FEA is also visible in the model, but the first peak is less pronounced and the second peak is slightly shifted closer to the transverse loading direction ($\pi/2$). For $\chi \approx 61$, the predicted angle of initiation of delamination growth of the model and FEA is approximately 101° and 112° respectively, where larger χ cause this angle to slightly shift towards $\pi/2$.

The mode decomposition of the ERR in mode I (blue), mode II (red) and mode III (magenta) contributions is provided in Figs. 8c and 8e for $\chi \approx 61$ and $\chi \approx 102$ respectively. Analysing Fig. 8c in detail, it can be seen that the first peak in ERR is almost purely mode II, whereas significant mode I contributions are present in the second peak, reaching almost similar magnitudes as mode II. Thus, growth will be initiated in the direction of the second peak in Figs. 8b and 8d. Mode-mixity agrees well between the analytical model and FEA, showing similar mode I and mode II contributions at the angle at which growth is initiated. Taking a closer look at Fig. 8b, it can be seen that mode II (in-plane shear) follows, besides minor quantitative deviations, the predictions of the 3D FEA. Very small out-of-plane shear contributions (mode III, $G^{III} < 0.05$ N/mm) are predicted by the analytical model and FEA. The minor shift in the second peak is associated with the peak of the opening mode I contributions occurring at a slightly smaller angle than in the FEA, which is also visible in Fig. 8e.

It should be noted that compared to 3D FEA very similar behaviour of the ERR and its components at the respective threshold strains are obtained, which underlines that deviations in threshold strain prediction relate to approximating the deformation behaviour of the buckle and thus requiring larger applied strains to access the deformation state (force and moment resultants at the delamination boundary) causing delamination propagation. Such approximations including the treatment of contact by a finite set of control points are deemed to cause the minor deviations in the angle of delamination propagation, which is discussed in detail in Section 5.

The behaviour of type B sublaminates ($[B] \neq 0, A_{I6} \neq 0, D_{I6} \neq 0$, $I = \{1, 2\}$) is described in an analogous manner to type A (Fig. 8) in Fig. 9. Threshold strain predictions of the stacking sequences considered ([45/0] – blue lines; [45/-45/0] – red lines) are provided in Fig. 9a. As for type A, mode-mix and mode I predictions of the analytical model bound the results of the 3D FEA. However, besides showing a similar qualitative behaviour, larger deviations in mixed-mode threshold strain predictions between model and FEA are present, which increase with larger diameter-to-thickness ratios (χ). All threshold strains and respective deviations are provided in Section 4.2.3 in Table 4.

Fig. 9a also shows a larger span in strain between a conservative mode I criterion (symbol ×) and mode-mix predictions (symbol □), since critical ERRs for the layups studied are significantly larger than for the configuration analysed for type A (Fig. 9a). This is visualized in Figs. 9b and 9d describing the behaviour of the ERR for [45/-45/0] at the onset of delamination growth. The maximum ERRs are 0.63 N/mm (model) and 0.60 N/mm (FEA) for $\chi \approx 68$ and 0.64 N/mm (model) and 0.59 N/mm (FEA) for $\chi \approx 95$. Predictions of the model are qualitatively similar to FEA, except of a step-like increase in ERR for $\chi \approx 68$.

The reason for the larger deviations in threshold strain prediction than for type A is provided in Figs. 9c and 9e describing the breakdown of the ERR in mode I (blue), mode II (red) and mode III (magenta). In FEA, peaks of mode I and mode II appear at almost the same location for $\chi \approx 68$ and coincide for $\chi \approx 95$, whereas predictions of the model show a larger offset in between these peaks causing larger critical ERRs and thus require more applied strain to initiate delamination growth. This discrepancy and its relation to both parts of the analytical model (energy approach to approximate post-buckling deformation and crack-tip element analysis) are discussed in Section 5.

Type C layups (off-axis unidirectional sublaminates) are analysed as type A and B considering the stacking sequence $[45_2]$. Good agreement between the analytical model and 3D FEA is obtained for threshold strains and the ERR. The respective findings in the form of Figs. 8 and 9 are provided in Appendix B.

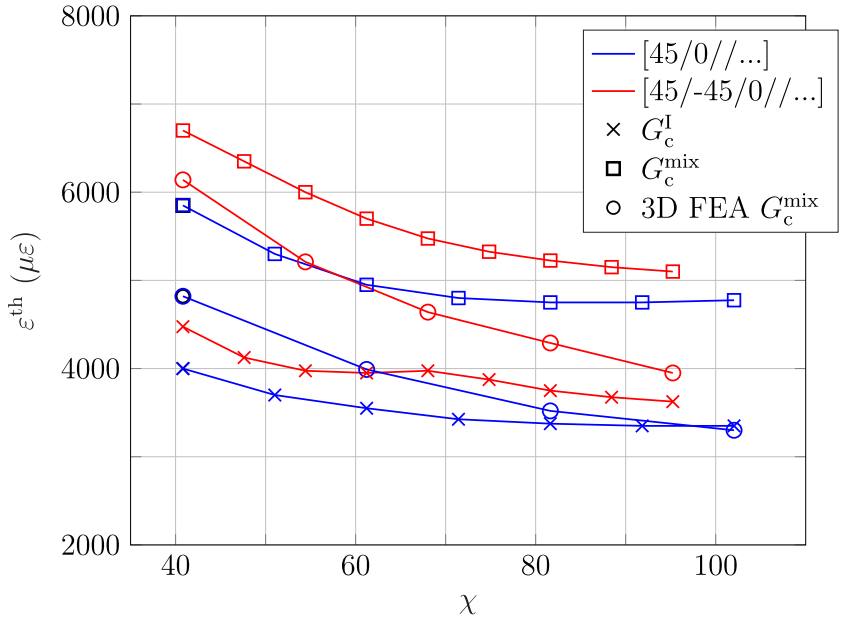
Next, for all configurations studied, threshold strains and critical ERRs are summarized in Section 4.2.3.

4.2.3. Summary of results

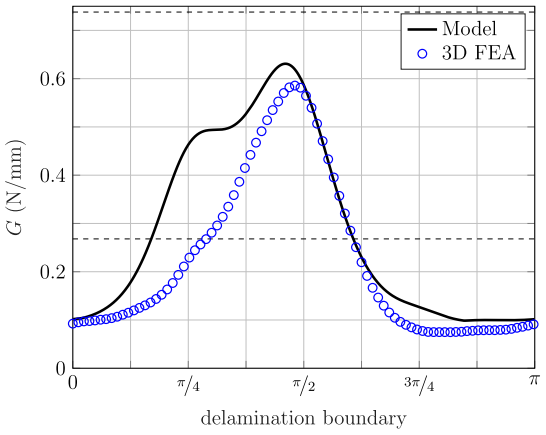
Table 4 lists threshold strains (ε^{th}) and critical ERRs (G_c^{mix}) determined with the aid of the analytical model for all types, layups and configurations for which 3D FEA simulations were also performed; data for the remaining configurations can be extracted from Figs. 8, 9 and B.1. Deviations between threshold strain predictions from the model and FEA are also provided in Table 4 as Δ.

With the aid of Table 4, the results obtained can be readily analysed and evaluated. Type A sublaminates ($B_{I6} \neq 0, A_{I6} = D_{I6} = 0, I = \{1, 2\}$) exhibit good agreement of threshold strains with FEA (within 13%), where the lowest and highest values of χ can be regarded as lower and upper bound of suitable configurations. Critical ERRs determined by the analytical model are in excellent agreement with FEA underlining that the model is capable of correctly describing the damage growth behaviour for these layups, which has been highlighted in Fig. 8. Thus, for type A, the small deviations in threshold strains are associated with the approximation of the displacement field employed in the energy formalism.

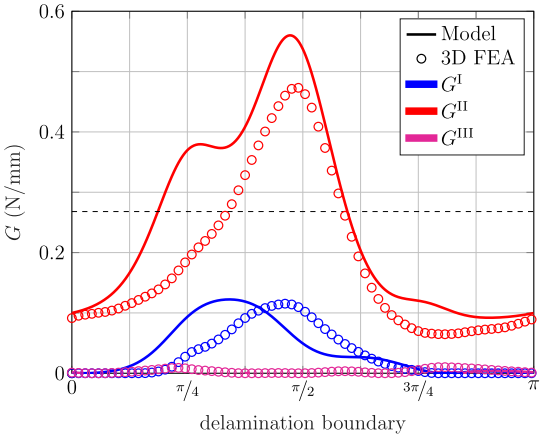
Type B sublaminates, *i.e.* a fully populated ABD matrix (full mechanical coupling), show significantly larger deviations in threshold strains than type A, where sublaminate [45/-45/0] exhibits better predictions than [45/0]. However, on analysing results of the critical ERRs G_c^{mix}, it becomes apparent that these deviations mainly relate to significantly larger critical ERRs determined in the analytical model,



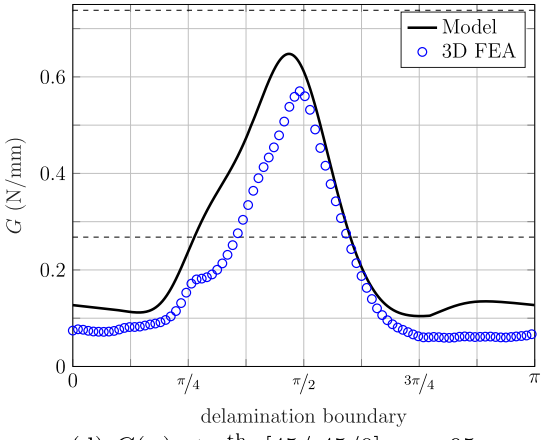
(a) Threshold strain $\varepsilon^{\mathrm{th}}$ predictions against χ for type B.



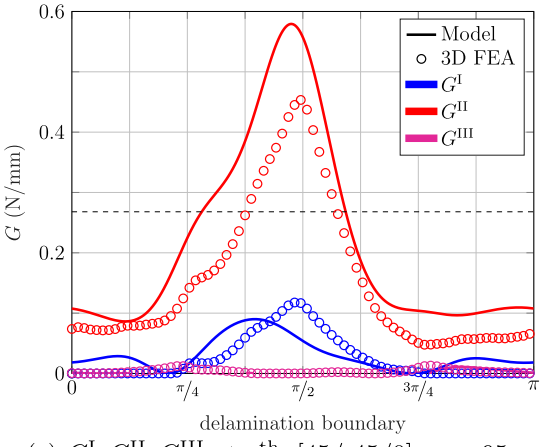
(b) $G(\varphi)$ at $\varepsilon^{\mathrm{th}}$, [45/-45/0], $\chi \approx 68$.



(c) $G^{\mathrm{I}}, G^{\mathrm{II}}, G^{\mathrm{III}}$ at $\varepsilon^{\mathrm{th}}$, [45/-45/0], $\chi \approx 68$.



(d) $G(\varphi)$ at $\varepsilon^{\mathrm{th}}$, [45/-45/0], $\chi \approx 95$.



(e) $G^{\mathrm{I}}, G^{\mathrm{II}}, G^{\mathrm{III}}$ at $\varepsilon^{\mathrm{th}}$, [45/-45/0], $\chi \approx 95$.

Fig. 9. Delamination growth behaviour of type B sublaminates, $\chi = \frac{2R}{at}$.

Table 4
Overview of threshold strains (ε^{th}) and critical ERRs (G_c^{mix}).

type	Layup	$\chi = \frac{2R}{at}$	Threshold strain ε^{th} ($\mu\varepsilon$)		Δ (%)	Crit. ERR G_c^{mix} (N/mm)	
			Model	3D FEA		Model	3D FEA
A	[45/-45]	41	10120	9000	12	0.44	0.43
		61	8490	7850	8	0.40	0.41
		82	7670	7280	5	0.43	0.43
		102	7710	6890	12	0.46	0.43
	[45/0/-45]	41	4590	4050	13	0.40	0.38
		54	3920	3590	9	0.41	0.39
		68	3520	3290	7	0.41	0.39
		81	3250	3070	6	0.42	0.40
		95	3250	2950	10	0.39	0.40
B	[45/0]	41	5850	4820	21	0.59	0.52
		61	4940	3990	24	0.64	0.51
		82	4730	3520	34	0.67	0.51
		102	4750	3360	41	0.69	0.49
	[45/-45/0]	41	6680	6140	9	0.58	0.56
		54	6000	5210	15	0.62	0.59
		68	5470	4640	18	0.62	0.58
		81	5210	4290	21	0.63	0.57
		95	5080	3960	28	0.64	0.57
C	$[45_2]$	41	9440	8820	7	0.34	0.38
		61	8500	7910	7	0.41	0.41
		82	8380	7520	11	0.45	0.41
		102	8350	7020	19	0.48	0.41

where deviations of G_c^{mix} between the analytical model and FEA are similar to deviations in threshold strains (for the majority of cases in type B). This indicates that for type B sublaminates the current form of the crack-tip element formalism misses contributions to the ERR, since the approximation of the post-buckling deformation was found to be basically unaffected by the type of sublaminate (*cf.* Section 4.2.1) and the qualitative behaviour of the ERR at the respective threshold strains agrees with FEA predictions (*cf.* Fig. 9).

For type C sublaminates ($[B] = 0, A_{I6} \neq 0, D_{I6} \neq 0, I = \{1, 2\}$), threshold strains agree well with FEA (within 11% except of $\chi \approx 102$) where the largest χ should also be regarded as an upper bound for suitable configurations. The increasing deviations are associated with increasing deviations in critical ERR, where smaller diameter-to-thickness ratios (χ) exhibit good agreement. Thus, even though significantly less pronounced than for type B and of minor relevance regarding threshold strain predictions in the range $40 < \chi < 100$ (assuming an inherent, almost constant deviation due to the approximation of the displacement field of the buckle), it appears that some contributions of the ERR are also missed for type C layups, which is discussed in detail in the subsequent section.

5. Discussion

Since the work presents a novel modelling approach and a comprehensive parametric study of buckling-driven delamination propagation, the current section discusses both in Sections 5.1 and 5.2, respectively.

5.1. Analytical model

The main objective of the current work has been the development of an analytical model that enables a localized analysis of the energy release rate (ERR) along the delamination boundary, thus accounting for localized delamination growth patterns observed in experiments [5,20,35], and considers mode-mixity. This is deemed essential regarding robust predictions of buckling-driven delamination propagation but could not be hitherto implemented in analytical approaches. Such a model has been achieved by employing a problem description in cylindrical coordinates and combining an energy approach, which employs a Rayleigh–Ritz formalism to approximate the post-buckling deformation, with a crack-tip element (CTE) analysis, which determines the ERR and its mode decomposition (mode I, mode II, mode III).

The energy approach considers full mechanical coupling, *i.e.* extension-shear, extension-bend, extension-twist/shear-bend, bend-twist, and contact of sublaminate and base laminate, which has been observed in experiments [20,27]. The problem description in cylindrical coordinates introduces a φ-dependence in the stiffness coefficients of the *ABD* matrix that significantly increases the complexity of the energy derivation. However, since a fully symbolic integration was achieved by performing algebraic manipulations in the software package Mathematica, this inherent complexity vanishes yielding the total potential energy as a function of generalized coordinates, loading parameters, material parameters and dimensions, *cf.* Eq. (11). With the total potential energy and respective equilibrium equations determined analytically, parametric studies can be efficiently performed and computational cost scales with the number of generalized coordinates used, where with the current configuration (see below) solution points require between 3 and 7 s (depending on the amount of zero entries in the *ABD* matrix) on a single core of an Intel(R) i7 processor.

The generalized coordinates used comprise the amplitudes of the trigonometric series employed to approximate the displacement field of the buckle. As described in Section 4.1, 240 generalized coordinates are considered. It should be stressed that significantly fewer generalized coordinates are required to describe the post-buckling behaviour only. Determining the ERR along the delamination boundary with the CTE analysis requires precise predictions of the force and moment resultants at the delamination front and thus require a more detailed approximation of the displacement field.

Contact in the form of hard contact is incorporated by defining control points in the area of the delamination enforcing the condition of out-of-plane displacements $w(r, \varphi) \geqslant 0$. A set of 10 points, including locations close to the boundary and approximately around the area of maximum buckling displacements of mode shapes without contact conditions in place, are considered and found to enforce reliably $w(r, \varphi) \geqslant 0$ to an error of $|0.01|$ mm for all laminates and configurations studied. However, it should be noted that more control points might slightly alter the buckling shape and thus deformations at the delamination boundary, but this effect is minor (test runs with up to 24 control points were performed) and also not expedient given the increasing computational cost with each added control point. With the contact condition, a set of 260 nonlinear equations govern the deformation behaviour of the buckle. Further extensions in the context of Kirchhoff–Love Plate Theory (2D deformations without out-of-plane shear contributions) are not expedient, where only marginal improvements come along significantly increasing (initial) computational cost. Even though results obtained for the configurations studied indicate a robust small deviation in threshold strain predictions associated with post-buckling deformation, if deemed necessary, extensions should rather focus on considering out-of-plane shear by approximating the rotations of the cross-section in light of Mindlin–Reissner plate theory.

Note that modelling local buckling responses (thin-film assumption), on the one hand, embodies a simplification by avoiding the description of the displacement field of the global/parent laminate, but on the other hand, poses more complex deformation characteristics such as localized buckling shapes (*cf.* Fig. 7a) due to contact than when global bending contributions are considered (*cf.* [22]). Larger applied strains are also required to cause delamination growth, when global bending is not present. These characteristics considerably increase the number of generalized coordinates required and thus encourage future extensions of the model to consider global bending deformations. The model may also be extended to study elliptical delamination shapes, as considered in [3,22,41], by expressing the delamination boundary in terms of the semi-major and semi-minor

axis and the angle φ, where it remains to be determined whether a symbolic integration can be achieved.

The second part of the analytical model, the CTE analysis (*cf.* [10,12]) is adapted to the current problem description. The description in cylindrical coordinates enables a straightforward implementation of force and moment resultants acting on the delamination boundary, where the different orientation of the coordinate system (compared to [12]) causes a sign change in the coupling stiffness B_{lJ} (and compliance b_{lJ}), with all other parts of the coefficients c_{ij} used to determine the ERR (*cf.* Appendix A) being the same as in [12]. The non-singular field (NSF) approach as described in [12] has been employed, where the mode-mix parameter Ω is directly determined from the delamination depth (formula provided in [10]) and remains constant for all thin-film delaminations at 24°. Besides the validation of the NSF approach by comparisons against multiple experiments in [10], the results for laminates considered as being most suitable for the CTE analysis (type A) verify the choice of Ω. For these layups (and also mostly type C), very good agreement with 3D FEA employing VCCT has been obtained for mode-mix and thus the critical ERR.

The CTE analysis enforces the requirement of crack-tip displacement continuity by assuming strains $\varepsilon_{\varphi\varphi}$ and curvatures κ_{yy}, κ_{xy} being zero. Considering $\kappa_{xy} = 0$ disables twisting deformation caused by the crack-tip moment m_{ct} (if $D_{16} \neq 0$) and by the crack-tip out-of-plane shear force $n_{\mathrm{ct}}^{\varphi}$ (if $B_{66} \neq 0$). Bend-twist ($D_{16} \neq 0$) and shear-twist coupling ($B_{66} \neq 0$) are present for type B laminates but not type A, which might indicate that contributions of the ERR are missed when studying type B laminates with the CTE analysis in its current form. However, it remains to be clarified whether the formalism can be extended to consider explicit contributions associated with D_{16} and B_{66} without contradicting the displacement continuity condition. The CTE analysis as employed in the current model description yields good predictions of critical ERRs for type A. Predictions for type C show good agreement for smaller diameter-to-thickness ratios χ, but the behaviour of the critical ERR with increasing χ indicates a similar trend as for type B. It should be noted that between the analytical model and 3D FEA deviations in threshold strain predictions beyond the range associated with post-buckling deformation (*cf.* type A in Table 4) are mostly associated with deviations in the critical ERR.

The analytical model significantly advances capabilities of current analytical approaches to describe buckling-driven delamination propagation. Studying the behaviour of the ERR and its components along the delamination boundary provides insight into the delamination growth characteristics (mode-mix, critical ERRs, alignment of mode contributions) and enables a better understanding about what causes larger compressive strength for certain layups (*e.g.* [45/-45]), which is discussed next.

5.2. Threshold strains and energy release rate

The analytical modelling approach provides the post-buckling deformation of the sublaminate and the behaviour of the ERR and its components (mode I, mode II, mode III) along the delamination boundary for uniaxial and biaxial in-plane far-field compressive loading in the form of applied strain. Biaxial loading is not addressed presently but its model implementation is used to account for transverse deformations of the parent laminate when subjected to uniaxial loading. With the behaviour of the ERR and its components determined, critical ERRs and corresponding threshold strains, *i.e.* applied strains causing the initiation of delamination growth, can be readily obtained.

Employing the Rayleigh–Ritz formalism in the modelling approach, it is expected that larger applied loads are associated with respective post-buckling deformations (*cf.* post-buckling paths in Fig. 6) when compared to 3D FEA, where inherent deviations decrease with more precise approximations (to a certain extent beyond which the constitutive behaviour should rather be refined). As described in Section 5.1, negligible improvements are expected by employing more than the currently used 240 generalized coordinates. As a consequence, regarding threshold strain predictions of the analytical model, deviations obtained for type A laminates, showing very similar critical ERRs compared to 3D FEA, are associated with deviations in the post-buckling deformation only. Thus, loads need to be increased by the respective deviations to attain the deformation state associated with delamination growth. Such a range of deviations is also present for other types of laminates, since it has been determined in Section 4.2.1 that the stacking sequence does not affect the quality of the approximation of the post-buckling deformation.

The range of diameter-to-thickness ratios investigated in the parametric study ($40 < \chi < 103$) relates to radii of delaminations ($R = \{8\text{-}28\}$ mm) which may be categorized as barely visible impact damage (BVID). It should be stressed that the current work does not attempt to reproduce CAI scenarios, where damage morphology is much more complex, but rather provide fundamental understanding of buckling-driven delamination growth in composite laminates. Hence, insight into features governing the laminate strength of delaminated laminates is obtained.

Threshold strain predictions presented should be treated as upper bound results, since global bending contributions will significantly increase the energy state of the plate and thus the ERR besides also causing larger mode I contributions. However, the thin-film treatment was deemed necessary in order to isolate the effect of stacking sequences and delamination size on the ERR and thus clearly identify the contribution of local buckling towards buckle-driven delamination propagation.

For type A stacking sequences, in comparison with 3D FEA, maximum deviations of up to 13% are present at lower and upper bounds of configurations studied, with deviations entirely below 10% for configurations inside these bounds. Based on the observations made, the analytical model in its current form can be directly used for design studies of stacking sequences characterized by type A, *i.e.* sublaminates which exhibit extension-twist/shear-bend coupling ($B_{I6} \neq 0$) but do not undergo extension-shear and bend-twist coupling ($A_{I6} = D_{I6} = 0$).

For type B laminates (with a fully populated *ABD* matrix), larger deviations in comparison with 3D FEA can be related to deviations in critical ERRs as described in Section 4.2.3. Considering such deviations as offsets, would allow for more precise threshold strain predictions which follow the qualitative behaviour of FEA predictions.

Laminates exhibiting extension-shear and bend-twist coupling ($A_{I6} \neq 0, D_{I6} \neq 0$) with $B_{lJ} = 0$, referred to as type C, are studied by the off-axis unidirectional layup $[45_2]$. Even though good agreement in threshold strains with FEA are obtained (except of the upper bound of configurations), further analysis into the deviating trend in critical ERRs is required before the modelling approach can be directly implemented in design.

Regarding quantitative measures of threshold strain, stacking sequences [45/-45] and $[45_2]$ clearly exhibit the highest values, which would underline their suitability for designing damage tolerant laminates. However, it was found in [9] that unidirectional sublaminates (on and off-axis) are prone to intra-ply cracking through the entire thickness of the sublaminate causing splitting failure before the initiation of delamination growth. Thus, a stacking sequence [45/-45] showing similar magnitudes compared to $[45_2]$ is therefore deemed more suitable. Besides intra-ply cracking, the susceptibility of the stacking sequences to delamination migration [5,6,30], should be considered in evaluating the damage tolerance of the laminates. In [20], delamination migration has been observed for [0/45] and [0/90/90] sublaminate but not for [45/-45].

The stacking sequence [45/0], considered when studying BVID and CAI strength of composites (*e.g.* [24,35]), shows significantly smaller threshold strains compared to [45/-45] and $[45_2]$, which stems from

undergoing larger post-buckling deformation due to softer material behaviour (smaller D_{IJ}) even though the critical ERRs are larger than for the other layups. It should be stressed that the large threshold strains of [45/-45] and $[45_2]$ relate, besides the sublaminate undergoing less post-buckling deformation, to a larger spread of ERR along the delamination boundary with peaks in mode I and mode II being not aligned. In contrast, the ERR for the case [45/0] is more localized with peaks of mode I and mode II being close to each other, where larger diameter-to-thickness ratios χ cause eventually alignment of mode I and mode II contributions (similar to the case [45/-45/0] shown in Fig. 9). It should be noted that [45/0] exhibits significantly better threshold strains compared to [0/45] (*cf.* case provided in Section 4.1, see [20], and corresponding configuration in Table 4), since the sign change in B_{IJ} causes a different contact scenario and affects crack-tip moments and forces.

It is also worth noting that considering a dominant delamination being present between the third and fourth layer, layups with the sequence [45/-45] on the outside still show better threshold strains than for [45/0], *cf.* [45/-45/0] with [45/0/-45] in Section 4.2.2. Such behavioural analysis of the ERR is enabled by the analytical model, which by running efficient parametric studies leads to in-depth understanding on how layups and deformation characteristics affect buckling-driven delamination growth.

6. Conclusions

Buckling-driven delamination propagation of multi-directional composite laminates has been analysed in detail with the aid of an analytical modelling approach that provides robust and efficient predictions of applied strains causing delamination growth, *i.e.* threshold strains, and the behaviour of the energy release rate (ERR) and its mode decomposition along the delamination boundary. The analytical model considers localized delamination growth, *i.e.* determining the ERR along the delamination boundary, and mode-mixity, which significantly advances current capabilities of analytical approaches. Beyond that, a precise approximation of the displacement field and incorporating contact conditions enables tracing of actual post-buckling paths, which has been validated by comparison with experiments.

After validating the analytical model against experimental results from [20,27], a parametric study of delaminations relating to dimensions observed in BVID and analysed in CAI tests has been performed for various multi-directional sublaminates considering a quasi-isotropic parent laminate. Based on extensive comparisons with three dimensional finite element analysis (3D FEA), the following conclusions can be drawn:

- The analytical model can be directly applied to design studies considering laminates categorized as type A, *i.e.* those with extension-twist coupling but no extension-shear and bend-twist coupling (*e.g.* [45/-45]), since excellent agreement in the behaviour of the ERR is obtained.
- Adequate and reliable estimates of threshold strain can be obtained for laminates categorized as type B, *i.e.* those with full mechanical coupling (*e.g.* [45/0]), if respective deviations in critical ERRs are offset. Employing the crack-tip element analysis, contributions in the ERR are arguably missing for this type of laminate which possibly relates to suppressing twisting deformation at the crack-tip.
- The analytical model provides good threshold strain predictions for laminates categorized as type C (*e.g.* off-axis unidirectional sublaminates such as $[45_2]$), *i.e.* those with extension-shear and bend-twist coupling, and the coupling stiffness matrix having zero coefficients only.

Furthermore, the effect of approximating the post-buckling deformation on the threshold strain predictions could be precisely determined by comparing post-buckling responses of laminates exhibiting various types of mechanical coupling and the behaviour of the ERR of laminates and configurations generating the same critical ERR. These deviations, deemed to be present for all laminates, are around 11–13% at lower and upper bounds of the diameter-to-thickness range considered and within 9% for configurations inside the bounds.

The parametric study, involving the analysis of the behaviour of the ERR along the delamination boundary, highlights why certain layups require significantly larger applied strains to cause delamination growth. Layups causing a wider spread of ERR along the boundary and exhibiting different locations in peaks for mode I and mode II, *e.g.* [45/-45] and $[45_2]$, also show the largest threshold strains. Considering sublaminates with three layers, larger threshold strains are also obtained, if the outer layers have a [45/-45] layup (compared to other possible layups using the quasi-isotropic parent laminates studied). With regards to designing damage tolerant laminates, besides buckling-driven delamination propagation, other damage mechanisms, such as intra-ply cracking (matrix cracks) and delamination migration, should be considered, which may diminish the benefits of the aforementioned stacking sequences. Aside from the addition of global bending deformations to the model, extensions to consider the aforementioned damage mechanisms should be targeted in the pursuit of further advancements in analytical models for predicting laminate strength under compressive loading and thus improving damage tolerant design of composite laminates.

Declaration of Competing Interest

The authors declare that they have no known competing financial interests or personal relationships that could have appeared to influence the work reported in this paper.

Acknowledgements

This project has received funding from the European Union's Horizon 2020 research and innovation programme under the Marie Skłodowska-Curie grant agreement No 842543.

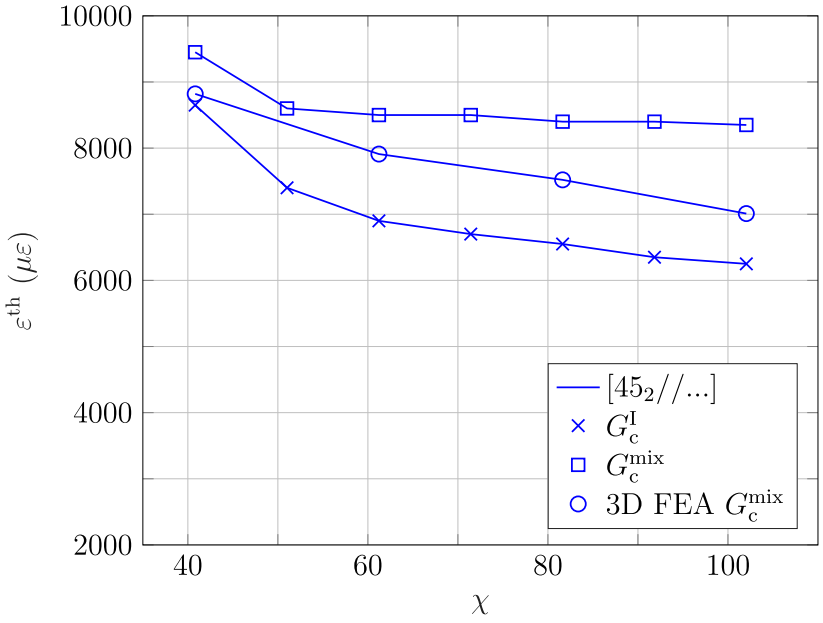
The author wants to thank Prof. Ahmer Wadee (Imperial College London) for fruitful scientific discussions, reviewing of the manuscript and ongoing support throughout the project.

Appendix A. Coefficients c_{ij} in the crack-tip element analysis

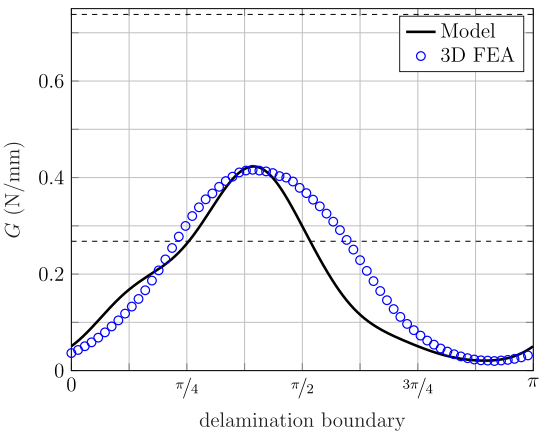
The coefficients c_{ij} used in Eq. (21) to determine the energy release rate (ERR) are obtained by inserting strains ($\varepsilon_{rr}, 2\varepsilon_{r\varphi}$) and curvature ($\kappa_{rr}$) of part ① and ② of the crack-tip element (*cf.* Eqs. (18) and (19)) into Eq. (20), where subsequent rearranging and collecting terms for the crack-tip forces (n^r_{ct}, n^φ_{ct}) and moment m_{ct} yields

$$
\begin{aligned}
c_{11} &= a^{①}_{11} + a^{②}_{11} - b^{①}_{11} at + b^{②}_{11}(1-a)t + d^{①}_{11}\left(\frac{at}{2}\right)^2 + d^{②}_{11}\left(\frac{(1-a)t}{2}\right)^2,\\
c_{22} &= d^{①}_{11} + d^{②}_{11},\\
c_{33} &= a^{①}_{66} + a^{②}_{66},\\
c_{12} &= b^{①}_{11} + b^{②}_{11} - d^{①}_{11}\left(\frac{at}{2}\right) + d^{②}_{11}\left(\frac{(1-a)t}{2}\right),\\
c_{13} &= a^{①}_{16} + a^{②}_{16} - b^{①}_{16}\left(\frac{at}{2}\right) + b^{②}_{16}\left(\frac{(1-a)t}{2}\right),\\
c_{23} &= b^{①}_{16} + b^{②}_{16},
\end{aligned}
\tag{A.1}
$$

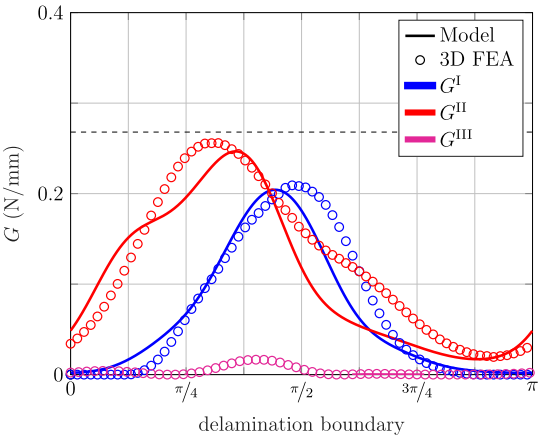
which are the same as provided in [12] except of the coupling compliances b_{11}, b_{16} having the opposite sign. This relates to the opposed z-direction (thickness direction, *cf.* Figs. 1 and 3) compared to [12] resulting in a sign change of the coupling stiffness entries (B_{IJ}).



(a) Threshold strain ε^{th} predictions against χ for type C ($[45_2]$).



(b) G at ε^{th}, $[45_2]$, $\chi \approx 61$.



(c) G^I, G^{II}, G^{III} at ε^{th}, $[45_2]$, $\chi \approx 61$.

Fig. B.1. Delamination growth behaviour of type C sublaminates, $\chi = \frac{2R}{at}$.

Appendix B. Type C – Threshold strains and ERR

Results of threshold strains and the behaviour of the energy release rate (ERR) along the delamination boundary are provided in Fig. B.1 for the sublaminate $[45_2]$ characterizing type C layups (unidirectional off-axis sublaminates, $[B] = 0$ but $A_{I6} \neq 0, D_{I6} \neq 0, I = \{1, 2\}$).

The behaviour of threshold strain (ε^{th}) against diameter-to-thickness ratio (χ) is shown in Fig. B.1a exhibiting good agreement between the analytical model and 3D FEA for smaller χ, where increasing deviations occur with larger χ; *cf.* Table 4 for numerical data and respective deviations. Despite showing significantly better predictions than type B (similar deviations as type A), in particular for $\chi < 100$, a similar trend as observed in type B sublaminates is also present for type C, where predictions of the 3D FEA show a stronger decrease in threshold strains with increasing χ compared to the analytical model.

The breakdown of the ERR is provided in Figs. B.1a and B.1b for $\chi \approx 61$. The excellent agreement in threshold strain for this configuration is demonstrated by both analytical model and 3D FEA determining roughly the same critical ERR ($G_c^{mix} = 0.41$ N/mm), which is equal to the maximum ERR in Fig. B.1a. The behaviour of the mode I, mode II and mode III contributions provided in Fig. B.1b shows good agreement for mode I and mode II with similar magnitudes of the respective peaks, where only minor differences in span of the peaks and respective locations of the maxima is present. As pointed out in Section 4.2.2 for sublaminate [45/-45] (type A), the large threshold strains obtained for $[45_2]$ relate to the peaks of mode I and mode II being not aligned, so that despite significant mode I contributions, large applied strains are required to cause delamination growth.

References

[1] Abir MR, Tay TE, Ridga M, Lee HP. Modelling damage growth in composites subjected to impact and compression after impact. Compos Struct 2017;168:13–25.
[2] Baker AA, Murray LS. Composite Materials for Aircraft Structures. AIAA Education Series; 2016.
[3] Baluch AH, Falcó O, Jiménez JL, Tijs BHAH, Lopes CS. An efficient numerical approach to the prediction of laminate tolerance to barely visible impact damage. Compos Struct 2019;225:111017.
[4] Benzeggagh ML, Kenane M. Measurement of mixed-mode delamination fracture toughness of unidirectional glassepoxy composites with mixed-mode bending apparatus. Compos Sci Tech 2013;56:439–49.

[5] Canturri C, Greenhalgh ES, Asp LE, Pinho ST. Fractographic study to characterise the interaction between intralaminar and interlaminar fracture from embedded defects under compression loading. Composites Part A 2019;125:105557.
[6] Canturri C, Greenhalgh ES, Pinho ST. Delamination growth directionality and the subsequent migration processes – the key to damage tolerant design. Composites Part A 2013;54:79–87.
[7] Chai H, Babcock CD, Knauss WG. One dimensional modelling of failure in laminated plates by delamination buckling. Int J Solids Struct 1981;17 (11):1069–83.
[8] Chai H, Knauss WG, Babcock CD. Observation of damage growth in compressively loaded laminates. Exp Mech 1983;23(3):329–37.
[9] Choudhry RS, Rhead AT, Nielsen MWD, Butler R. A plate model for compressive strength prediction of delaminated composites. Compos Struct 2019;210:509–17.
[10] Davidson BD, Gharibian SJ, Yu L. Evaluation of energy release rate-based approaches for predicting delamination growth in laminated composites. Int J Fract 2000;105:343–65.
[11] Davidson BD, Hurang H, Schapery RA. An analytical crack-tip element for layered elastic structures. J Appl Mech-T ASME 1995;62:294–305.
[12] Davidson BD, Yu L, Yu L, Hu H. Determination of energy release rate and mode mix in three-dimensional layered structures using plate theory. Int J Fract 2000;105:81–104.
[13] Harvey CM, Wood JD, Wang S, Watson A. A novel method for the partition of mixed-mode fractures in 2D elastic laminated unidirectional composite beams. Compos Struct 2014;116:589–94.
[14] Hutchinson JW, Suo Z. Mixed mode cracking in layered materials. Adv Appl Mech 1992;29:63–191.
[15] Jane KC, Yin W-L. Refined buckling and postbuckling analysis of two-dimensional delamination—II. Results for anisotropic laminates and conclusion. Int J Solids Struct 1992;29(5):611–39.
[16] Kachanov LM. Separation failure of composite materials. Poly Mech 1976;12 (5):812–5.
[17] Köllner, A, An analytical framework for the structural stability analysis of damageable structures and its application to delaminated composites. Dissertation, Technische Universität Berlin; 2017.
[18] Köllner A, Forsbach, F, Völlmecke C, Delamination buckling in composite plates: an analytical approach to predict delamination growth. In: Abali, B. E., Altenbach, H., dell'Isola, F., Eremeyev, V., Öchsner, A. (Eds.), New Achievements in Continuum Mechanics and Thermodynamics. Vol. 108 of Advanced Structured Materials. Springer; 2019.
[19] Köllner A, Kashtalyan M, Guz I, Völlmecke C. On the interaction of delamination buckling and damage growth in cross-ply laminates. Int J Solids Struct 2020;120–121:912–28.
[20] Köllner A, Nielsen MWD, Srisuriyachot J, Rhead AT, Butler R. Buckle-driven delamination models for laminate strength prediction and damage tolerant design. Thin-Walled Struct 2021;161:107468.
[21] Köllner A, Völlmecke C. An analytical framework to extend the general structural stability analysis by considering certain inelastic effects—theory and application to delaminated composites. Compos Struct 2017;170:261–70.
[22] Köllner A, Völlmecke C. Post-buckling behaviour and delamination growth characteristics of delaminated composite plates. Compos Struct 2018;203:777–88.
[23] Krueger R. Virtual crack closure technique: History, approach, and applications. Appl Mech Rev 2004;57(2):109–43.
[24] Lin S, Thorsson SI, Waas AM. Predicting the low velocity impact damage of a quasi-isotropic laminate using est. Compos Struct 2020;112530.
[25] Lopes CS, Sádaba S, Gonz'alez C, Llorca J, Camanho PP. Physically-sound simulation of low-velocity impact on fiber reinforced laminates. Int J Impact Eng 2016;92:3–17.
[26] Nettles AT, Douglas MJ. A comparison of quasi-static indentation testing to low velocity impact testing, composite materials: Testing, design and acceptance criteria. Standard. American Society for Testing and Materials; 2000.
[27] Nilsson K-F, Asp LE, Alpman JE, Nystedt L. A theoretical and experimental investigation of buckling induced delamination growth. J Mech Phys Solids 1993;41(4):749–82.
[28] Nilsson K-F, Asp LE, Alpman JE, Nystedt L. Delamination buckling and growth for delaminations at different depths in a slender composite panel. Int J Solids Struct 2001;38:3039–71.
[29] Ouyang T, Sun W, Guan Z, Tan R, Li Z. Experimental study on delamination growth of stiffened composite panels in compression after impact. Compos Struct 2018;206:791–800.
[30] Pernice MF, De Carvalho NV, Ratcliffe JG, Hallett SR. Experimental study on delamination migration in composite laminates. Composites Part A 2015;73:20–34.
[31] Reddy JN. Mechanics of laminated composite plates and shells: theory and analysis. CRC Press; 2004.
[32] Schapery RA, Davidson BD. Prediction of energy release rate for mixed-mode delamination using classical plate theory. Appl Mech Rev 1990;43(5):281–7.
[33] Shi Y, Swait T, Soutis C. Modelling damage evolution in composite laminates subjected to low velocity impact. Compos Struct 2012;94:2902–13.
[34] Sun XC, Hallet SR. Barely visible impact damage in scaled composite laminates: Experiments and numerical simulations. Int J Impact Eng 2017;109:178–95.
[35] Sun XC, Hallet SR. Failure mechanisms and damage evolution of laminated composites under compression after impact (CAI): experimental and numerical study. Composites Part A 2018;104:41–59.
[36] Tan W, Falzon BG, Chiu LNS, Price M. Predicting low velocity impact damage and compression-after-impact(CAI) behaviour of composite laminates. Composites Part A 2016;71:212–26.
[37] Abaqus, Providence RI, USA: Dassault Systèmes; 2019.
[38] Thompson JMT, Hunt GW. A general theory of elastic stability. John Wiley & Sons; 1973.
[39] Tuo H, Lu Z, Ma X, Xing J, Zhang C. Damage and failure mechanism of thin composite laminates under low-velocity impact and compression-after-impact loading conditions. Composites Part B 2019;163:642–54.
[40] Wang K, Zhao L, Hong H, Gong Y, Zhang J, Hu N. An analytical model for evaluating the buckling, delamination propagation, and failure behaviors of delaminated composites under uniaxial compression. Compos Struct 2019;223:110937.
[41] Wang K, Zhao L, Hong H, Zhang J, Hu N. An extended analytical model for predicting the compressive failure behaviors of composite laminate with an arbitrary elliptical delamination. Int J Solids Struct 2020.
[42] Wolfram Research Inc, 2020. Mathematica, Version 12.0. Champaign, IL.
[43] Wood JD, Harvey CM, Wang S. Partition of mixed-mode fractures in 2D elastic orthotropic laminated beams under general loading. Compos Struct 2016;149:239–46.
[44] Xia F, Jian F, Zhu Z, Li P, Liang H, Jin F. A modified first order shear deformation theory for reissner-mindlin composite panels with internal delamination. Compos Struct 2019;224:110935.